JOURNAL OF THE AMERICAN CHEMICAL SOCIETY

Article

Spectroscopic and Electronic Structure Studies of Intermediate X in Ribonucleotide Reductase R2 and Two Variants: A Description of the Fe-Oxo Bond in the Fe–O–Fe Dimer

Nataa Miti, Michael D. Clay, Lana Saleh, J. Martin Bollinger,, and Edward I. Solomon

J. Am. Chem. Soc., **2007**, 129 (29), 9049-9065• DOI: 10.1021/ja070909i • Publication Date (Web): 29 June 2007

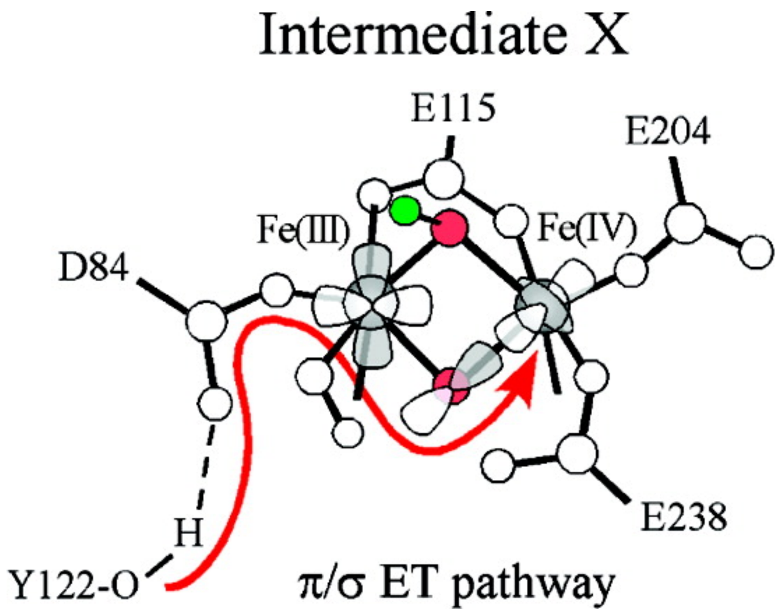

Journal of the American Chemical Society is published by the American Chemical Society. 1155 Sixteenth Street N.W., Washington, DC 20036

JACS
ARTICLES

Spectroscopic and Electronic Structure Studies of Intermediate X in Ribonucleotide Reductase R2 and Two Variants: A Description of the Fe^{IV}-Oxo Bond in the Fe^{III}−O−Fe^{IV} Dimer

Nataša Mitić,[†,§] Michael D. Clay,[†] Lana Saleh,[‡] J. Martin Bollinger, Jr.,*,[‡] and Edward I. Solomon*,[†]

Contribution from the Department of Chemistry, Stanford University, Stanford, California 94305, and Department of Biochemistry and Molecular Biology, The Pennsylvania State University, University Park, Pennsylvania 16802

Received February 13, 2007; E-mail: edward.solomon@stanford.edu; jmb21@psu.edu

Abstract: Spectroscopic and electronic structure studies of the class I *Escherichia coli* ribonucleotide reductase (RNR) intermediate **X** and three computationally derived model complexes are presented, compared, and evaluated to determine the electronic and geometric structure of the Fe^{III}−Fe^{IV} active site of intermediate **X**. Rapid freeze−quench (RFQ) EPR, absorption, and MCD were used to trap intermediate **X** in R2 wild-type (WT) and two variants, W48A and Y122F/Y356F. RFQ-EPR spin quantitation was used to determine the relative contributions of intermediate **X** and radicals present, while RFQ-MCD was used to specifically probe the Fe^{III}/Fe^{IV} active site, which displayed three Fe^{IV} d−d transitions between 16 700 and 22 600 cm^{-1}, two Fe^{IV} d−d spin-flip transitions between 23 500 and 24 300 cm^{-1}, and five oxo to Fe^{IV} and Fe^{III} charge transfer (CT) transitions between 25 000 and 32 000 cm^{-1}. The Fe^{IV} d−d transitions were perturbed in the two variants, confirming that all three d−d transitions derive from the d-π manifold. Furthermore, the Fe^{IV} d-π splittings in the WT are too large to correlate with a bis-μ-oxo structure. The assignment of the Fe^{IV} d−d transitions in WT intermediate **X** best correlates with a bridged μ-oxo/μ-hydroxo [Fe^{III}(μ-O)(μ-OH)Fe^{IV}] structure. The μ-oxo/μ-hydroxo core structure provides an important σ/π superexchange pathway, which is not present in the bis-μ-oxo structure, to promote facile electron transfer from Y122 to the remote Fe^{IV} through the bent oxo bridge, thereby generating the tyrosyl radical for catalysis.

1. Introduction

Binuclear non-heme iron-containing active sites are found in a large number of enzymes that perform highly specific oxidation reactions involving binding and activation of dioxygen.[1−3] This class of enzymes includes hemerythrin (reversible O_2 binding),[4,5] soluble methane monooxygenase (sMMO, hydroxylation of methane),[6,7] stearoyl acyl carrier protein Δ^9-desaturase (Δ^9D, fatty acid desaturation),[8−10] and the R2 subunit of class I ribonucleotide reductase (RNR, generation of stable tyrosyl radical).[11−14] Current research centers on understanding the structural and electronic features of the binuclear iron clusters that govern the diverse reactivity of these enzymes with O_2. Crystal structures exist for many proteins in this class in oxidized and/or reduced forms.[15−17] Each protein contains carboxylate and histidine ligands that coordinate the binuclear iron core responsible for the reductive activation of O_2, generating similar peroxo-diferric and high-valent iron-oxo intermediates that have been observed and characterized in some of these enzymes.[18−23]

[†] Stanford University.

[‡] Pennsylvania State University.

[§] Current address: Department of Chemistry, University of Queensland, St. Lucia, QLD 4072, Australia.

(1) Solomon, E. I.; Brunold, T. C.; Davis, M. I.; Kemsley, J. N.; Lee, S. K.; Lehnert, N.; Neese, F.; Skulan, A. J.; Yang, Y. S.; Zhou, J. *Chem. Rev.* **2000**, *100*, 235−349.
(2) Nordlund, P.; Eklund, H. *Curr. Opin. Struct. Biol.* **1995**, *5*, 758−766.
(3) Wallar, B. J.; Lipscomb, J. D. *Chem. Rev.* **1996**, *96*, 2625−2657.
(4) Brunold, T. C.; Solomon, E. I. *J. Am. Chem. Soc.* **1999**, *121*, 8277−8287.
(5) Brunold, T. C.; Solomon, E. I. *J. Am. Chem. Soc.* **1999**, *121*, 8288−8295.
(6) Merkx, M.; Kopp, D. A.; Sazinsky, M. H.; Blazyk, J. L.; Muller, J.; Lippard, S. J. *Angew. Chem., Int. Ed.* **2001**, *40*, 2782−2807.
(7) Fox, B. G.; Froland, W. A.; Jollie, D. R.; Lipscomb, J. D. *Method Enzymol.* **1990**, *188*, 191−202.
(8) Schmidt, H.; Heinz, E. *Plant Physiol.* **1990**, *94*, 214−220.
(9) Wada, H.; Schmidt, H.; Heinz, E.; Murata, N. *J. Bacteriol.* **1993**, *175*, 544−547.
(10) Fox, B. G.; Lyle, K. S.; Rogge, C. E. *Acc. Chem. Res.* **2004**, *37*, 421−429.
(11) Reichard, P.; Ehrenberg, A. *Science* **1983**, *221*, 514−519.
(12) Nordlund, P.; Eklund, H. *J. Mol. Biol.* **1993**, *232*, 123−164.
(13) Stubbe, J. *Curr. Opin. Chem. Biol.* **2003**, *7*, 183−188.
(14) Nordlund, P.; Reichard, P. *Annu. Rev. Biochem.* **2006**, *75*, 681−706.
(15) Nordlund, P.; Sjoberg, B. M.; Eklund, H. *Nature* **1990**, *345*, 593−598.
(16) Rosenzweig, A. C.; Nordlund, P.; Takahara, P. M.; Frederick, C. A.; Lippard, S. J. *Chem. Biol.* **1995**, *2*, 632.
(17) Elango, N.; Radhakrishnan, R.; Froland, W. A.; Wallar, B. J.; Earhart, C. A.; Lipscomb, J. D.; Ohlendorf, D. H. *Protein Sci.* **1997**, *6*, 556−568.
(18) Bollinger, J. M., Jr.; Edmondson, D. E.; Huynh, B. H.; Filley, J.; Norton, J. R.; Stubbe, J. *Science* **1991**, *253*, 292−298.
(19) Bollinger, J. M., Jr.; Tong, W. H.; Ravi, N.; Huynh, B. H.; Edmondson, D. E.; Stubbe, J. *Methods Enzymol.* **1995**, *258*, 278−303.
(20) Liu, K. E.; Valentine, A. M.; Wang, D. L.; Huynh, B. H.; Edmondson, D. E.; Salifoglou, A.; Lippard, S. J. *J. Am. Chem. Soc.* **1995**, *117*, 10174−10185.
(21) Lee, S. K.; Nesheim, J. C.; Lipscomb, J. D. *J. Biol. Chem.* **1993**, *268*, 21569−21577.
(22) Broadwater, J. A.; Ai, J. Y.; Loehr, T. M.; Sanders-Loehr, J.; Fox, B. G. *Biochemistry* **1998**, *37*, 14664−14671.

10.1021/ja070909i CCC: $37.00 © 2007 American Chemical Society

Scheme 1. Reaction Mechanism of O_2 Activation and Tyrosyl Radical (Y122•) Generation from the *E. coli* Class I RNR R2 Binuclear Iron Site

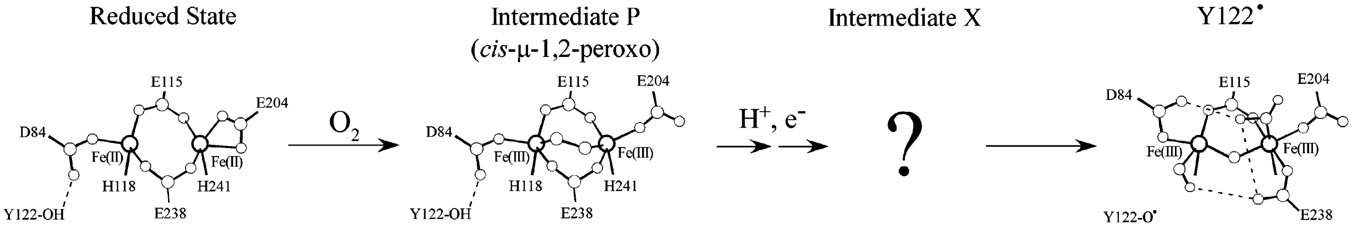

Ribonucleotide reductase catalyzes the rate-limiting step in DNA biosynthesis in all organisms, the reduction of ribonucleotides to their corresponding deoxyribonucleotides.[13,14] The R1 subunit of the *Escherichia coli* RNR holoenzyme R1•R2 complex contains the ribonucleotide catalytic active site, whereas the R2 subunit contains the binuclear Fe^{II} active site, which (along with an exogenous electron) reductively activates O_2 resulting in one-electron oxidation of an endogeneous Y122 residue to form a tyrosyl radical and an oxo-bridged diferric cluster, as shown in Scheme 1. The generation of this stable $Y122^{\bullet}$ makes R2 active to initiate a long-range (~35 Å) proton coupled electron transfer (PCET), between the two subunits, to the catalytic active site in the R1 subunit.[24] This leads to the formation of a thiyl radical on C439 of R1 and ultimately nucleotide reduction.[25]

Crystal structures of both reduced and oxidized R2-WT and several variants combined with spectroscopy have greatly contributed toward the understanding of the binuclear non-heme iron active site.[12,15] The active site structures of both diferrous and diferric R2-WT are shown in Figure 1. In the fully reduced form of R2-WT (see Figure 1A), the two iron centers are separated by a distance of 3.9 Å, with the Fe1 being 4C and Fe2 being 5C, as supported by MCD spectroscopy.[26,27] The two carboxylate residues, Glu115 and Glu238, bridge the two Fe centers in a μ-1,3 fashion, and the rest of the coordination is completed by His118 and monodentate Asp84 on Fe1 and bidentate Glu204 and His241 on the Fe2 center. Tyr122, which gets oxidized to the stable radical, is ~5 Å away from Fe1 and is H-bonded to Asp84.[28−30] The major change during the conversion of the binuclear iron cluster from diferrous to diferric form involves a significant reorganization of two carboxylates, Glu238 and Asp84. In oxidized R2-WT (see Figure 1B), both Fe centers become 6C with an Fe−Fe distance of 3.3 Å. There is one bridging μ-1,3 carboxylate from Glu115 and a single μ-oxo bridge (from O_2)[31] between the two Fe^{III} centers. Fe1 is coordinated to His118, bidentate Asp84, and a terminal solvent molecule (water or hydroxide), whereas Fe2 coordination is completed by His241, monodentate Glu204 and Glu238, and a terminal solvent molecule.

Major efforts have been directed toward defining the structural and electronic properties of high valent iron-oxo intermediates, specifically in sMMO and R2.[1,6,32−34] sMMO catalyzes the two-electron oxidation of methane to methanol, and both intermediates P or H_{peroxo} (peroxo Fe^{III}_2 complex) and Q (Fe^{IV}_2 species) have been trapped and kinetically characterized in sMMO.[20,21] The methane-hydroxylating intermediate, Q, characterized by Mössbauer and EXAFS spectroscopies, exhibits an $S = 0$ diamagnetic ground state and is thought to contain a bis-μ-oxo core structure with two antiferromagnetically coupled Fe^{IV} ions at an Fe−Fe distance of 2.46 Å.[35] For R2, there is evidence for the formation of a *cis*-μ-1,2-peroxo Fe^{III}_2 intermediate similar to P in D84E variants of the *E. coli* protein and the WT protein from mouse.[23,36] During the assembly of the R2 binuclear iron in the presence of O_2, an intermediate **X** (an oxo-bridged Fe^{III}-Fe^{IV} species) has been identified kinetically and spectroscopically (by stopped-flow, EPR, ENDOR, EXAFS, and RFQ-MCD).[19,28,37−41] The latter decays to give the stable $Y122^{\bullet}$ and oxo-bridged diferric cluster. Mössbauer spectroscopy was consistent with **X** containing two inequivalent iron sites, a high-spin Fe^{III} ($S = {}^5/_2$) antiferromagnetically coupled to a high-spin Fe^{IV} ($S = 2$) yielding a resultant $S_{tot} = {}^1/_2$ spin system.[19,28] This magnetic coupling between the two iron atoms is also evident from a nearly isotropic $S = {}^1/_2$ EPR signal at $g = 2$. The short distance between the two iron atoms in intermediate **X** (2.5 Å) determined from EXAFS[37] results in combination with ^{17}O and $^{1,2}H$ ENDOR spectroscopy[39,40] indicated the presence of at least one μ-oxo bridge, with the second oxygen atom being coordinated to the Fe^{III} site as a terminal water or hydroxide. The presence of two additional bridging ligands (carboxylates) in either a μ-1,1 or μ-1,3 bridging mode has also been inferred. The spectroscopic data on both intermediate **X** and **Q** are of high interest as both have distinctly short Fe−Fe distances with the spectra implicating a different number of bridging oxo ligands. Alternatively, a number of computational analyses,[33,42−52]

---

(23) Skulan, A. J.; Brunold, T. C.; Baldwin, J.; Saleh, L.; Bollinger, J. M., Jr.; Solomon, E. I. *J. Am. Chem. Soc.* **2004**, *126*, 8842−8855.
(24) Stubbe, J.; Nocera, D. G.; Yee, C. S.; Chang, M. C. Y. *Chem. Rev.* **2003**, *103*, 2167−2201.
(25) Licht, S. S.; Stubbe, J. *FASEB J.* **1995**, *9*, A1320−A1320.
(26) Yang, Y. S.; Baldwin, J.; Ley, B. A.; Bollinger, J. M., Jr.; Solomon, E. I. *J. Am. Chem. Soc.* **2000**, *122*, 8495−8510.
(27) Wei, P. P.; Skulan, A. J.; Mitić, N.; Yang, Y. S.; Saleh, L.; Bollinger, J. M., Jr.; Solomon, E. I. *J. Am. Chem. Soc.* **2004**, *126*, 3777−3788.
(28) Ravi, N.; Bollinger, J. M., Jr.; Huynh, B. H.; Edmondson, D. E.; Stubbe, J. *J. Am. Chem. Soc.* **1994**, *116*, 8007−8014.
(29) Bollinger, J. M., Jr.; Tong, W. H.; Ravi, N.; Huynh, B. H.; Edmondson, D. E.; Stubbe, J. *J. Am. Chem. Soc.* **1994**, *116*, 8024−8032.
(30) Bollinger, J. M., Jr.; Tong, W. H.; Ravi, N.; Huynh, B. H.; Edmondson, D. E.; Stubbe, J. *J. Am. Chem. Soc.* **1994**, *116*, 8015−8023.
(31) Ling, J. S.; Sahlin, M.; Sjoberg, B. M.; Loehr, T. M.; Sanders-Loehr, J. *J. Biol. Chem.* **1994**, *269*, 5595−5601.
(32) Solomon, E. I. *Inorg. Chem.* **2001**, *40*, 3656−3669.
(33) Siegbahn, P. E. M. *Chem. Phys. Lett.* **2002**, *351*, 311−318.
(34) Gherman, B. F.; Baik, M. H.; Lippard, S. J.; Friesner, R. A. *J. Am. Chem. Soc.* **2004**, *126*, 2978−2990.
(35) Shu, L. J.; Nesheim, J. C.; Kauffmann, K.; Munck, E.; Lipscomb, J. D.; Que, L. *Science* **1997**, *275*, 515−518.
(36) Yun, D.; Garcia-Serres, R.; Chicalese, B. M.; An, Y. H.; Huynh, B. H.; Bollinger, J. M., Jr. *Biochemistry* **2007**, *46*, 1925−1932.
(37) Riggs-Gelasco, P. J.; Shu, L. J.; Chen, S. X.; Burdi, D.; Huynh, B. H.; Que, L.; Stubbe, J. *J. Am. Chem. Soc.* **1998**, *120*, 849−860.
(38) Mitić, N.; Saleh, L.; Schenk, G.; Bollinger, J. M., Jr.; Solomon, E. I. *J. Am. Chem. Soc.* **2003**, *125*, 11200−11201.
(39) Willems, J. P.; Lee, H. I.; Burdi, D.; Doan, P. E.; Stubbe, J.; Hoffman, B. M. *J. Am. Chem. Soc.* **1997**, *119*, 9816−9824.
(40) Burdi, D.; Willems, J. P.; Riggs-Gelasco, P.; Antholine, W. E.; Stubbe, J.; Hoffman, B. M. *J. Am. Chem. Soc.* **1998**, *120*, 12910−12919.
(41) Bollinger, J. M., Jr.; Chen, S. X.; Parkin, S. E.; Mangravite, L. M.; Ley, B. A.; Edmondson, D. E.; Huynh, B. H. *J. Am. Chem. Soc.* **1997**, *119*, 5976−5977.
(42) Siegbahn, P. E. M. *Inorg. Chem.* **1999**, *38*, 2880−2889.
(43) Lovell, T.; Li, J.; Noodleman, L. *J. Biol. Inorg. Chem.* **2002**, *7*, 799−809.
(44) Torrent, M.; Vreven, T.; Musaev, D. G.; Morokuma, K.; Farkas, O.; Schlegel, H. B. *J. Am. Chem. Soc.* **2002**, *124*, 192−193.

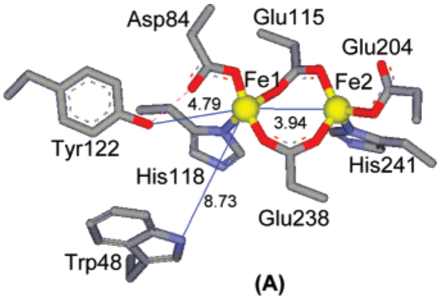

(A)
Wild type (WT) R2 from *E. coli*
reduced

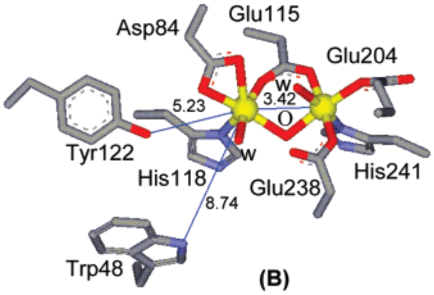

(B)
Wild type (WT) R2 from *E. coli*
oxidized

Figure 1. Crystal structures of the (A) reduced binuclear active site of R2-WT (1XIK) and (B) oxidized binuclear active site of R2-WT (1RIB) from *E. coli*. Specific H-bonding interactions that are crucial for R2 reactivity are shown in purple (dotted line). The structures were generated using the crystallographic coordinates from the indicated PDB files.

including the most recent study by Noodleman and co-workers,[53] have concluded that **X** contains a bis-μ-oxo core structure, similar to the proposed structure of intermediate **Q** in sMMO.

Thus, the structure of **X** remains to be determined, and the geometric and electronic description of **X** is required to understand the mechanism of tyrosyl radical formation in RNR. Recently, we developed a rapid-freeze-quench magnetic circular dichroism technique (RFQ-MCD) to probe electronic and structural properties of intermediate **X**, utilizing a double variant of RNR (Y122F/Y356F), which allowed for the generation of up to 1.4 equiv of **X**.[38] These MCD data permitted direct detection of the high-spin Fe^{IV} spin-allowed and forbidden ligand field transitions.

In the present study RFQ-MCD is used in combination with low temperature (LT) absorption, VTVH MCD, and EPR spectroscopies to obtain a detailed experimental description of the ligand−metal bonding in the catalytically active $Fe^{III}-Fe^{IV}$ binuclear site of **X** in the R2 subunit of RNR in WT and two variants, a double variant Y122F/Y356F and a single variant W48A. In R2-WT, **X** forms in a second-order reaction between the biferrous active site and O_2 with a rate constant of $k_{form} = 2.1 \pm 0.2 \times 10^5$ mol^{-1} s^{-1} and decays with a rate constant of $k_{decay} = 1.0 \pm 0.2$ s^{-1} at 5 °C, whereas, in R2 Y122F/Y356F, **X** had a formation rate constant of $k_{form} = 5 \pm 1 \times 10^4$ mol^{-1} s^{-1} and $k_{decay} = 0.3 \pm 0.1$ s^{-1} at 11 °C.[54,55] Thus, the replacement of easily oxidizable Y122 and Y356 residues with phenylalanines leads to high yields of pure **X** (up to 1.4 equiv) with increased lifetime. The decay of **X** in the R2-Y122F/Y356F variant generates a tyrosyl radical from one of the nearby tyrosine residues in the protein, as it cannot oxidize F122. The crucial role of W48 in the ET process of R2 has been recently investigated.[54−57] In both W48F and W48A variants of R2, a diradical intermediate species containing both intermediate **X** and $Y122^{\bullet}$ (**X**-$Y122^{\bullet}$) is formed from a preceding Fe_2O_2 complex with a $k_{form} = 7.5 \pm 2.5$ s^{-1} and with a $k_{decay} = 0.18 \pm 0.04$ s^{-1}.[54−57] The kinetic parameters and the $Y122^{\bullet}$ production stoichiometry for the R2-W48A variant are very similar to those reported earlier for R2-W48F.[55] These experimental data presented here are complemented by DFT, TD-DFT, ΔSCF, and Slater transition state calculations to examine the ligand field transition energies of the Fe^{IV} site to correlate to three possible model core structures for **X**: mono-μ-oxo, μ-oxo/μ-hydroxo, and bis-μ-oxo (*vide infra*). This study correlates the experimental spectroscopic data with DFT calculations to elucidate the fundamental features of the Fe^{IV}-oxo bond in **X**, understand the effects of the geometric perturbations on the $Fe^{III}-O-Fe^{IV}$ unit, and evaluate its geometric and electronic structural contributions to the formation of $Y122^{\bullet}$.

2. Experimental Section

All commercial reagents of the highest grade were used as obtained without further purification: enzyme grade 4-(2-hydroxyethyl)-1-piperazineethanesulfonic acid (HEPES) (Aldrich), ferrous ammonium sulfate (Mallinckrodt), glycerol (Aldrich), d_3-glycerol (98 atom % D, Cambridge Isotope Laboratories), and deuterium oxide (99.9 atom % D, Aldrich). HEPES buffer (100 mM, pH 7.6) was degassed with at least three freeze−pump−thaw cycles at 10^{-3} Torr, while the apo protein samples (on ice) were degassed by gentle flushing with O_2-scrubbed argon gas on the Schlenk line for at least 30 min at 4 °C. Solid ferrous ammonium sulfate was made anaerobic by pumping at 10^{-3} Torr for 30 min.

2.1. Preparation of apo R2-WT, R2-Y122F/Y356F, and R2-W48A. The apo form of R2-WT, Y122F/Y356F, and W48A variants was overexpressed, purified, and characterized as previously reported.[54−59]

2.2. Preparation of Intermediate X RFQ-MCD and RFQ-EPR Samples. The preparation of the differous R2 cluster was carried out under strictly anaerobic conditions in an argon filled Vacuum Atmospheres Company (Hawthorne, CA) glovebox (<1 ppm O_2). Once apo protein samples (1.0−1.6 mM) were deoxygenated on a Schlenk line at 4 °C, they were preloaded with 3.3−3.5 equiv of Fe^{II} (ferrous ammonium sulfate) dissolved in an anaerobic solution of 5 mM H_2SO_4 (neutralized with excess buffer), both with and without 5 mM

---

(45) Torrent, M.; Musaev, D. G.; Basch, H.; Morokuma, K. *J. Comput. Chem.* **2002**, *23*, 59−76.
(46) Han, W. G.; Lovell, T.; Liu, T. Q.; Noodleman, L. *Inorg. Chem.* **2003**, *42*, 2751−2758.
(47) Liu, T. Q.; Lovell, T.; Han, W. G.; Noodleman, L. *Inorg. Chem.* **2003**, *42*, 5244−5251.
(48) Siegbahn, P. E. M. *Q. Rev. Biophys.* **2003**, *36*, 91−145.
(49) Han, W. G.; Lovell, T.; Liu, T. Q.; Noodleman, L. *Inorg. Chem.* **2004**, *43*, 613−621.
(50) Liu, T. Q.; Lovell, T.; Han, W. G.; Noodleman, L. *Inorg. Chem.* **2004**, *43*, 6858−6858.
(51) Han, W. G.; Liu, T. Q.; Lovell, T.; Noodleman, L. *J. Am. Chem. Soc.* **2005**, *127*, 15778−15790.
(52) Han, W. G.; Liu, T. Q.; Lovell, T.; Noodleman, L. *J. Inorg. Biochem.* **2006**, *100*, 771−779.
(53) Han, W. G.; Liu, T. Q.; Lovell, T.; Noodleman, L. *Inorg. Chem.* **2006**, *45*, 8533−8542.
(54) Baldwin, J.; Krebs, C.; Ley, B. A.; Edmondson, D. E.; Huynh, B. H.; Bollinger, J. M., Jr. *J. Am. Chem. Soc.* **2000**, *122*, 12195−12206.
(55) Krebs, C.; Chen, S. X.; Baldwin, J.; Ley, B. A.; Patel, U.; Edmondson, D. E.; Huynh, B. H.; Bollinger, J. M., Jr. *J. Am. Chem. Soc.* **2000**, *122*, 12207−12219.
(56) Saleh, L.; Krebs, C.; Ley, B. A.; Naik, S.; Huynh, B. H.; Bollinger, J. M., Jr. *Biochemistry* **2004**, *43*, 5953−5964.
(57) Saleh, L.; Kelch, B. A.; Pathickal, B. A.; Baldwin, J.; Ley, B. A.; Bollinger, J. M., Jr. *Biochemistry* **2004**, *43*, 5943−5952.
(58) Parkin, S. E.; Chen, S. X.; Ley, B. A.; Mangravite, L.; Edmondson, D. E.; Huynh, B. H.; Bollinger, J. M., Jr. *Biochemistry* **1998**, *37*, 1124−1130.
(59) Saleh, L.; Bollinger, J. M., Jr. *Biochemistry* **2006**, *45*, 8823−8830.

ascorbate. The samples were allowed to equilibrate for 5 min prior to loading into an RFQ syringe. The second RFQ syringe was loaded with an O_2-saturated 100 mM HEPES buffer (1.5 mM O_2, 4 °C).

All RFQ samples were prepared using an Update Instruments System 1000 (Madison, WI) equipped with a Wiskind Grid Mixer and a spraying nozzle. Intermediate **X** was generated by quenching 20−50 μL of the anaerobic diferrous R2-WT, R2-Y122F/Y356F, and R2-W48A enzyme against an equal volume of O_2-saturated 100 mM HEPES buffer, pH = 7.6. This step was repeated multiple times to accumulate enough sample for MCD and EPR. The samples were freeze-quenched by spraying directly into liquid nitrogen or into liquid nitrogen cooled isopentane at −140 °C using appropriate reaction times (100−125 ms for R2-WT at 5 °C, 70−100 ms at 11 °C for R2-Y122F/Y356F, and 350−450 ms at 5 °C for R2-W48A). These aging reaction times used for trapping **X** were chosen based on previous stopped-flow kinetic studies.[57−59] The samples of the R2-W48A variant also contained 10% glycerol. The best results were achieved by freeze-quenching ~20−50 μL of the reaction mixture (diferrous protein samples and O_2-saturated 100 mM HEPES buffer, pH = 7.6). A wide mouth shallow liquid nitrogen container was used for quenching the samples directly in liquid nitrogen by placing the spraying nozzle ~5 mm above the surface of the liquid nitrogen. The reaction was initiated immediately upon placing the spraying nozzle in its position. After mixing, samples were ejected rapidly from the spray nozzle, freezing before rising to the surface of the liquid nitrogen (the samples came into contact with the walls of the dewar only after freezing). The frozen samples are small, flat ice crystals (~2−3 mm in size; in contrast samples frozen in chilled isopentane formed a slurry). Higher ram velocities (up to 3.2 cm/s) produced the best quality crystals. The reproducibility was verified by repeating the experiment for each sample numerous times (all the spectra shown are a result of at least eight independent experiments). Freezing samples of R2 in chilled isopentane (−140 °C) led to the formation of poor glasses (with light depolarization of ~10−15%) that limit the measurements of quantitative MCD spectral data. However, MCD spectra collected for corresponding samples frozen in liquid N_2 and isopentane were identical (see Figures S3 and S4 in the Supporting Information). RFQ frozen samples required for EPR analysis were packed into 4 mm quartz EPR tubes using long packers. The protocol for generation of an RFQ-MCD sample was described previously.[38] In brief, the frozen crystals of the intermediate were crushed into a fine powder in a container immersed in liquid nitrogen and then mixed thoroughly with glycerol (premeasured volume) at −30 °C in dry ice/ethanol bath until a homogeneous sample was obtained. To ensure homogeneity of the RFQ-MCD samples, the light beam in the MCD experiments was focused on at least 10 different regions of each MCD sample glass, and independent spectra were recorded. The MCD cell was carefully assembled on dry ice (two brass pieces with the 3.2 mm neoprene spacer and two infrasil quartz disks) with the intermediate frozen ice crystals/glycerol mixed paste being distributed evenly over the quartz disk of the MCD cell. The paste of intermediate **X** was then sandwiched between the two quartz disks, and the cell quickly froze in liquid nitrogen. All RFQ-MCD samples of intermediate **X** contained ~60−70% glycerol, and the final samples ranged in Fe concentration from 0.3 to 0.8 mM. The whole MCD sample preparation took on average 2−3 min. The stability of **X** in R2-WT and the two R2 variants was tested by monitoring the EPR signal of **X** over a 2−15 min time course at −30 °C since all RFQ-MCD samples were prepared at this temperature.

2.3. RFQ-EPR Experiments. All X-band (9.3 GHz) EPR spectra were obtained with a Bruker ER 220-D-SRC spectrometer equipped with an Air Products Model LTR Helitran liquid helium transfer refrigerator and a Lake Shore Cryotronics temperature controller model DTC-500 and an ESR-900 helium flow cryostat. The EPR signals were monitored at different temperatures ranging from 100 to 3 K using an ESR-900 cryostat and an external vacuum pump for temperatures below 4.2 K. Specific sample conditions and spectrometer conditions are given in figure legends. Spin quantitation of EPR samples was determined from integrated EPR signal intensities using 1 mM copper perchlorate as a standard.

2.4. RFQ-MCD Spectroscopy. MCD spectra were recorded on JASCO J810 (UV−visible region) and J200 (NIR region) spectropolarimeters, each equipped with an Oxford Instruments SM4-7T superconducting magnetocryostat capable of magnetic fields up to 8 and 7 T, respectively, and temperatures down to 1.4 K, using an S-20 photomultiplier tube (UV−vis, 900−300 nm) and a liquid-nitrogen-cooled InSb solid-state detector (NIR, 2000−600 nm). All MCD samples were checked for light depolarization effects by comparing the CD signal of a nickel (+)-tartrate solution placed before and after the sample. The depolarization was <5% at 1.8 K for all samples. All LT absorption and MCD spectra were simultaneously fit to Gaussian band shapes using the program PeakFit version 4 (AISN Software Inc.). VTVH MCD data were fit using an in-house program, which minimizes the χ^2 value by fitting the effective transition moment products with either a Simplex or a Levenberg−Marquadt algorithm with a spin Hamiltonian for the ground state Kramer's doublet $S = {}^1/_2$.[60]

2.5. LT Absorption Spectroscopy. Low-temperature absorption spectra were collected on a Cary-17 double-beam spectrometer equipped with a Janis Super Vari-Temp liquid helium cryostat at 10.0 K.

2.6. Computational. All density functional theory (DFT) calculations were performed on dual-CPU Pentium Xeon 2.8 GHz work stations employing spin-unrestricted (SU) and broken symmetry (BS) methods[61−63] to allow for a reasonable description of the electronic structure of antiferromagnetically coupled systems. All three models were geometry optimized using the Amsterdam Density Functional (ADF) program, version 2003.01 developed by Baerends et al.[64,65] A triple-ζ Slater-type orbital basis set (ADF basis set TZP) with a single polarization function at the local density approximation of Vosko, Wilk, and Nusair[66] with nonlocal gradient corrections of Becke and Perdew (BP86)[67,68] were employed. The molecular orbitals were plotted using gOpenMol version 2.32 and Molden version 4.1. ΔSCF and Slater transition state methods were employed using ADF. The Mulliken population analyses were performed using the AOMix[69] and PyMOlyze[70] programs. Time-dependent DFT (TD-DFT) calculations were performed with the Gaussian 03 package.[71] A 6-311G* basis set was used for all atoms with the local density approximation of Vosko, Wilk, and Nusair[66] and the nonlocal gradient corrections of Becke and Perdew (BP86).[67,68] In all models, the high-spin Fe antiferromagnetic (AF) state was initially converged with smaller basis sets (i.e., 3-21G*), which was used as the initial guess for larger basis sets (i.e., 6-311G*). The high-spin AF state for all models was found to be lower in energy than the low-spin AF state. Complete coordinates of all the geometry-optimized models discussed in the text are included in the Supporting Information (Tables S1−S3).

3. Results

3.1. EPR Characterization of RFQ Samples. All the RFQ-MCD samples of **X** used in the analysis were characterized by RFQ-EPR spectroscopy to establish the % **X** and % Y122$^\bullet$

---

(60) Solomon, E. I.; Pavel, E. G.; Loeb, K. E.; Campochiaro, C. *Coord. Chem. Rev.* **1995**, *144*, 369−460.
(61) Noodleman, L.; Case, D. A.; Aizman, A. *J. Am. Chem. Soc.* **1988**, *110*, 1001−1005.
(62) Noodleman, L. *J. Chem. Phys.* **1981**, *74*, 5737−5743.
(63) Noodleman, L.; Davidson, E. R. *Chem. Phys.* **1986**, *109*, 131−143.
(64) Baerends, E. J.; Ellis, D. E.; Ros, P. *Chem. Phys.* **1973**, *2*, 41−51.
(65) Velde, G. T.; Baerends, E. J. *J. Comput. Phys.* **1992**, *99*, 84−98.
(66) Vosko, S. H.; Wilk, L.; Nusair, M. *Can. J. Phys.* **1980**, *58*, 1200−1211.
(67) Becke, A. D. *J. Chem. Phys.* **1986**, *84*, 4524−4529.
(68) Perdew, J. P. *Phys. Rev. B* **1986**, *33*, 8822−8824.
(69) (a) Gorelsky, S. I. *AOMIX program*, revision 6.04 (http://www.sg-chem.net/). (b) Gorelsky, S. I.; Lever, A. B. P. *J. Organomet. Chem.* **2001**, *635*, 187−196.
(70) Tenderholt, A. L. *PyMOlyze*, version 1.04., http://pymolyze.sourceforge.net.
(71) Frisch, M. J., et al. *Gaussian 03*, revision C.02; Gaussian, Inc.: Wallingford, CT, 2004.

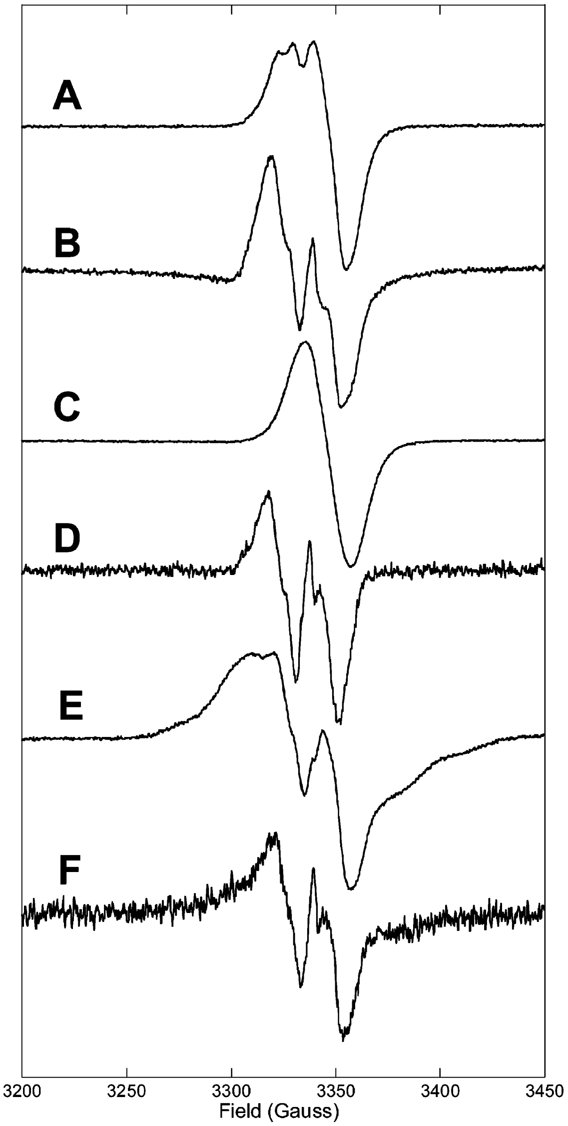

Figure 2. RFQ-EPR spectra of (A) the intermediate **X** in R2-WT (relative ratio of **X** and Y122$^{\bullet}$ 0.62:0.42), (C) in R2-Y122F/Y356F (98−100% **X**), and (E) the **X**−Y$^{\bullet}$ (79%) diradical species, formed in the reaction of apo enzymes with Fe^{II} and O_2, in comparison with EPR spectra of decayed intermediate **X** in R2-WT, R2-Y122F/Y356F, and R2-W48A (B, D, and F). The EPR spectra of decayed **X** were obtained by allowing the samples of **X** to thaw at room temperature for 10 min prior to freezing in liquid nitrogen. The spectrometer conditions for data acquisition were as follows: microwave frequency 9.38 GHz, temperature 3.0 K, microwave power 10 μW, modulation frequency 100 kHz, modulation amplitude 4 G, and receiver gain of 2.24×10^4.

present. Figure 2 shows the comparison of the EPR spectra of **X** trapped in R2-WT and the two variants Y122F/Y356F and W48A, with their corresponding decayed **X** spectra. The characteristic signal of **X** observed in both R2-WT (Figure 2A) and the double variant (Figure 2C) is typical of a system with the ground state $S_{\mathrm{tot}} = {}^1/_2$ and nearly isotropic $g = 2.0$ value. The aging times (110−125 ms) used for the formation of **X** in the R2-WT enzyme allowed for maximum amounts of **X** to be formed with as little of decayed products as possible, but variable amounts of the reaction product Y122$^{\bullet}$ were also detected (from 28 to 42%). This was unavoidable for the R2-WT reaction since the MCD sample manipulations were carried out at −30 °C following RFQ trapping in order to obtain good quality optical samples of **X**. The **X** intermediate was found to decay faster in the R2-WT enzyme than in the two R2 variants.

Figure 2A shows the EPR spectrum of **X** in R2-WT containing 62% ± 2% **X** and 38% ± 2% Y122$^{\bullet}$. The 10-min time point of the reaction was used as a reference spectrum of magnetically isolated Y122$^{\bullet}$ (see Figure 2B). A freeze-quenched sample from the reaction of the double variant with O_2 was used as a reference sample for **X** as its kinetics of **X** formation and decay are such that pure **X** accumulates in high yields (1.4 equiv) without contamination from Y122$^{\bullet}$ (Figure 2C). A slight excess of dithionite was used to eliminate any W48$^{+\bullet}$ species, which can accumulate by supplying an additional electron to form **X** under reductant-limiting conditions. The EPR spectrum of decayed **X** in the double variant is characteristic of a tyrosyl radical (Figure 2D). Finally, the EPR spectrum of **X** in the W48A variant exhibits a unique feature with a broader $g = 2.0$ signal (Figure 2E). This EPR signal is attributed to a coupled biradical species containing both **X** and Y122$^{\bullet}$. This EPR spectrum is not the same as that of magnetically isolated intermediate **X** or isolated Y122$^{\bullet}$ indicating a weak interaction of the two paramagnetic species, **X** and Y122$^{\bullet}$.[54,72] Subsequent decay of **X**-Y122$^{\bullet}$ in W48A gives an EPR spectrum characteristic of isolated Y122$^{\bullet}$ (Figure 2F). EPR spin quantitation for the W48A variant indicates that ~0.25 equiv of stable Y122$^{\bullet}$ is formed at the end of the reaction.

3.2. Low-Temperature Absorption and MCD Spectroscopy of Intermediate X. The low-temperature (LT) absorption spectra of **X** in R2-WT, R2-Y122F/Y356F, and R2-W48A are shown in Figure 3. The predominant spectral features of intermediate **X** in the 10 K absorption spectrum occur in the high-energy region centered at ~27 800 cm^{-1} ($\epsilon \approx 2800\ M^{-1}\ cm^{-1}$) with a steep increase in intensity starting at ~31 000 cm^{-1} ($\epsilon \approx 4000\ M^{-1}\ cm^{-1}$). There is also a rather weak tailing absorption feature at ~20 000 cm^{-1} ($\epsilon \approx 900\ M^{-1}\ cm^{-1}$). In the case of the R2-W48A variant, there is also a sharp feature in the absorption spectrum at ~24 000 cm^{-1} (Figure 3C) indicative of the presence of Y122$^{\bullet}$ that is weakly spin coupled to **X** (*vide supra*). A smaller similar sharp feature is present in the absorption spectrum of R2-WT-**X** (Figure 3A), but here the amount of Y122$^{\bullet}$ species correlates with the amount of decayed **X** quantitated by EPR. Consistent with the EPR results in Figure 2, no sharp Y122$^{\bullet}$ feature is present in the absorption spectrum of **X** for the R2-Y122F/Y356F variant.

The 10 K absorption spectra of decayed **X** in the R2-WT reaction and the two R2 variants are shown in the Supporting Information (Figure S1). Decay of **X** generates a μ-oxo bridged diferric cluster (broad absorption bands at ~31 250 and ~27 000 cm^{-1}) and the tyrosyl radical characterized by a sharp feature at ~24 330 cm^{-1}. The high-energy absorption features of **X** are difficult to differentiate from those attributed to decayed **X** (particularly in WT) since both **X** and the diferric cluster absorb in the region ~27 000−28 000 cm^{-1} and the primary difference lies in the kinetics of the band formation and disappearance. However, MCD spectroscopy allows for a complete differentiation of these bands, as the diferric cluster is not paramagnetic and will not exhibit intense LT MCD features (*C*-terms). Since intermediate **X** is paramagnetic, it shows an intense VTVH MCD signal.

---

(72) $J \approx 0.1\ cm^{-1}$.

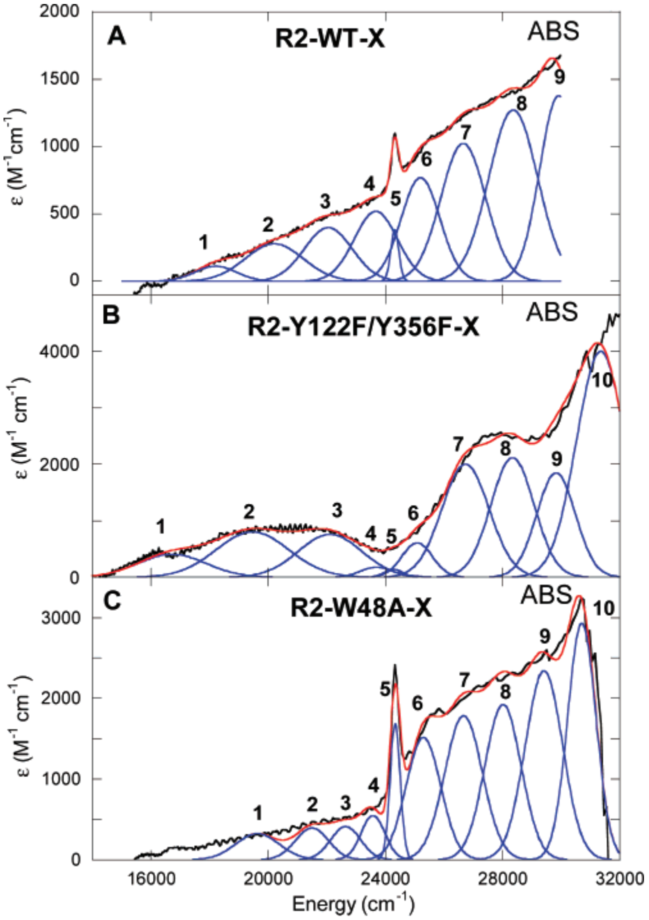

Figure 3. Low temperature (10 K) absorption spectra of intermediate **X** in (A) R2-WT, (B) R2-Y122F/Y356F, and (C) R2-W48A including simultaneous Gaussian fitting with their respective MCD data.

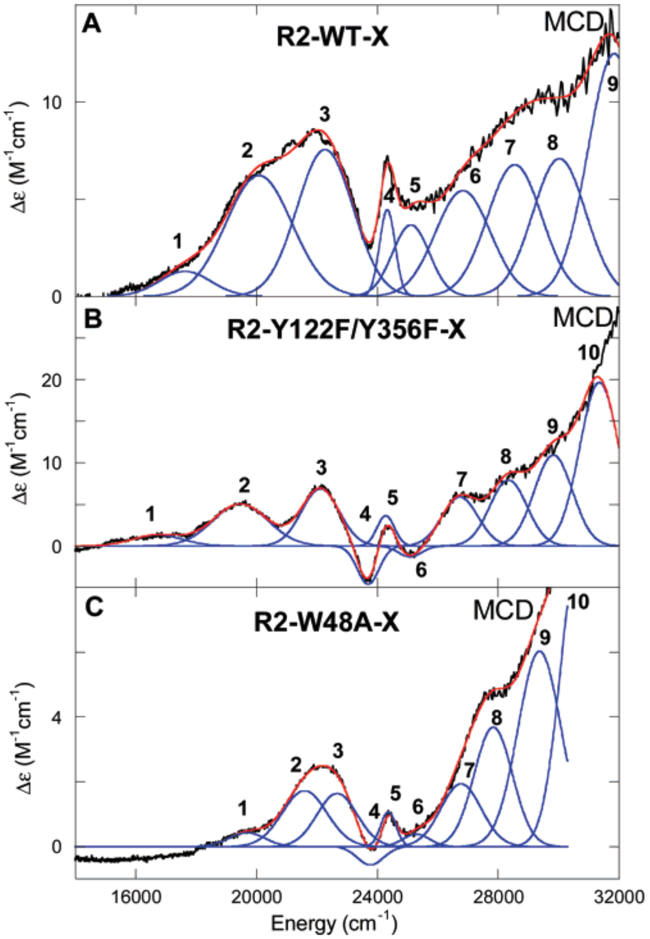

Figure 4. Low-temperature RFQ-MCD (1.8 K, 7 T) spectra of intermediate **X** in (A) R2-WT, (B) R2-Y122F/Y356F, and (C) R2-W48A including simultaneous Gaussian fitting with their respective absorption spectra.

Table 1. Experimental Transition Energies (cm^{-1}), C_0/D_0 Ratio, and Assignment of Intermediate **X** Transitions in (a) Wild-Type, (b) Y122F/Y356F, and (c) W48A[a]

	(a) wild-type	(b) Y122F/Y356F	(c) W48A		
band	ν_{max} (cm^{-1})	ν_{max} (cm^{-1})	ν_{max} (cm^{-1})	C_0/D_0	assignment
1	17 630	16 700	19 680	0.0062	Fe^{IV} d → d
2	20 080	19 460	21 590	0.0117	Fe^{IV} d → d
3	22 260	22 100	22 660	0.0170	Fe^{IV} d → d
4	23 530	23 690	23 760	0.0492	Fe^{IV} d → d spin flip
5	24 320	24 270	24 360	0.0502	Fe^{IV} d → d spin flip
6	25 110	25 080	25 280	0.0040	oxo → Fe^{IV}
7	26 830	26 730	26 770	0.0055	oxo → Fe^{IV}
8	28 540	28 340	27 840	0.0069	oxo → Fe^{IV}
9	30 020	29 820	29 370	0.0110	oxo → Fe^{III} or Fe^{IV}
10	31 840	31 350	30 670	0.0092	oxo → Fe^{III} or Fe^{IV}

[a] Fit parameters were determined using simultaneous Gaussian resolution of the LT absorption and MCD spectra, from Figures 3 and 4.

Figure 4 displays the low-temperature MCD spectra of **X** in R2-WT, R2-Y122F/Y356F, and R2-W48A. Figures 3B and 4B reproduce the absorption and MCD data obtained previously on R2-Y122F/Y356F-**X**. There is a good correlation of band signs, energies, and shapes between the three MCD spectra of intermediate **X**, and these can be correlated to the features observed in the absorption spectra. The simultaneous Gaussian fitting of the MCD with the LT absorption data results in 10 electronic transitions in the region from 5000 to 33 300 cm^{-1} (Table 1; note that no transitions are observed in the NIR region below 14 000 cm^{-1} associated with intermediate **X**). The LT-MCD data show an apparent large deviation from the MCD "sum rule" (equal and opposite signed LT-MCD intensity) and the deviation requires spin−orbit coupling of low-lying excited states into the ground state. The MCD and absorption spectra have been divided into three regions based on the intensities and C_0/D_0 ratios for **X** in R2-WT and the two R2 variants. C_0/D_0 ratios ($C_0/D_0 = k_BT/\mu_BB\ (\Delta\epsilon/\epsilon)_{max}$ where k_B is Boltzmann's constant, μ_B is the Bohr magneton ($k_B/\mu_B = 1.489$ K^{-1} T^{-1}), T is the temperature in K, ϵ is the molar absorptivity in M^{-1} cm^{-1}, and $\Delta\epsilon$ is the MCD intensity maximum in M^{-1} cm^{-1} recorded in the linear $1/T$ region) are used to differentiate a metal-based ligand field (d → d transitions) from ligand-based charge transfer (CT) transitions. Since the spin−orbit coupling constant for the Fe^{IV} is much higher ($\xi_{Fe}{}^{IV} = 520$ cm^{-1}) than that for the oxygen (60−70 cm^{-1}) or nitrogen (50 cm^{-1}) ligands, the d → d LF transitions are expected to have higher C_0/D_0 ratios as they are centered on the Fe^{IV} of intermediate **X**.[73,74] Region I (bands 1−3 in Figures 3 and 4) displays the most intense features in the MCD spectrum of **X**, with high C_0/D_0 ratios from 0.012 to 0.050 (i.e., high MCD, but weak absorption intensity). Thus,

---

(73) Solomon, E. I.; Hanson, M. A. In *Inorganic Electronic Structure and Spectroscopy*; Solomon, E. I., Lever, A. B. P., Eds.; John Wiley & Sons: New York, 1999; Vol. 2, pp 1−129.

(74) The high-spin Fe^{III} d−d LF transitions are all spin-forbidden.

these three bands (bands 1−3) can be assigned as the spin-allowed ligand field transitions of the high-spin Fe^{IV}, supporting significant Fe^{IV} character in the paramagnetic center of **X**.

Region II (bands 4 and 5) involves spin-forbidden LF transitions ($\Delta S = 1$ spin-flip transitions). These sharp but weak MCD bands are observed between 23 000 and 24 500 cm^{-1} and do not vary over any of the MCD spectra for **X** in R2-WT and the two variants. Based on the energy and bandwidth these transitions could be assigned to a spin flip on either the Fe^{III} or Fe^{IV} center. The ligand field independent spin-forbidden transitions gain some intensity in coupled dimers through the exchange interaction associated with the bridging ligand (*vide infra*). The ligand field independent spin flips of an Fe^{III} center (involving the ${}^6A_1 \rightarrow {}^4A_1$, ${}^4E$ transitions) are well-known to occur in the region of ~21 000 cm^{-1} in mono-μ-oxo ferric dimers and in the region 17 700−19 100 cm^{-1} for bis-μ-oxo ferric dimers.[75] Bands 4 and 5 are too high in energy to be attributed to Fe^{III} spin flips and are thus assigned as ligand field independent spin-forbidden transitions (${}^5E \rightarrow {}^3T_1$) on Fe^{IV}.

Region III (bands 6−10) involves transitions at ≥25 000 cm^{-1} with low C_0/D_0 ratios from 0.004 to 0.011 (i.e., weak MCD, but strong absorption) and are thus assigned as oxo-to-Fe^{IV} and oxo-to-Fe^{III} CT transitions. Oxo → Fe^{IV} transitions are anticipated to be at a lower energy relative to oxo → Fe^{III} CT due to the increased Z_{eff}. Modestly intense oxo → Fe^{III} CT transitions in mono-μ-oxo ferric dimers are observed at ≥28 000 cm^{-1}.[75] Jorgensen's optical electronegativity differences between the donor and acceptor orbitals can be used to estimate charge-transfer transition energies.[76] Using rough estimates of optical electronegativities (χ_{opt}) for high-spin Fe^{IV} ($\chi_{opt}(Fe^{IV}) = 2.8-3.2$) and a bridging oxo ligand ($\chi_{opt}(O^{2-}) = 3.6-3.8$) in the following expression:

$$\nu_{CT} = 30\,000\ [\chi_{opt}(O^{2-}) - \chi_{opt}(Fe^{IV})]\ cm^{-1}\ (LMCT)$$

calculates the oxo → Fe^{IV} CT transitions in the range 24 000−28 000 cm^{-1}. The same expression for high-spin Fe^{III} ($\chi_{opt}(Fe^{III}) = 2.5-2.7$) gives oxo → Fe^{III} CT transitions in the range 27 000−33 000 cm^{-1}. Therefore, it is reasonable to assume that bands 6 and 7 and possibly 8 in the MCD spectrum of **X** can be assigned as oxo → Fe^{IV} CT transitions and that the higher energy transitions could correspond to oxo → Fe^{III} CT transitions. However, this approach assumes the Fe^{III}-oxo and the Fe^{IV}-oxo bonding are mutually exclusive and neglects covalency effects over the entire Fe^{III}−O−Fe^{IV} dimer unit (*vide infra*).

The absorption and MCD spectra of decayed **X** in R2-WT and the two variants are given in the Supporting Information (Figure S1 and S2). These spectra are distinctly different from those of intermediate **X** in Figure 4 and provide additional evidence for the assignment of the spectral features in Figure 4 as due solely to **X**. The tyrosyl radical and μ-oxo bridged diferric cluster are the major decay products of **X** with the tyrosyl radical being the primary paramagnetic component. The MCD spectrum of decayed **X** in R2-WT enzyme exhibits a feature at ~24 300 cm^{-1} due to tyrosyl radical formation (note that this feature is different from that observed in this energy region for **X**). There is also a broad negative feature observed at ~20 000 cm^{-1} which is due to some paramagnetic decay contribution, not yet identified. The high-energy band at ~30 000 cm^{-1} is temperature independent (*B*-term MCD intensity) and arises from the diamagnetic contribution of the oxo-bridged diferric cluster. The decayed **X** of the R2-Y122F/Y356F variant exhibits the characteristic tyrosyl radical feature at ~24 300 cm^{-1} (Figure S2B) and the high-energy band at ~30 000 cm^{-1} which is also temperature independent.[28−30]

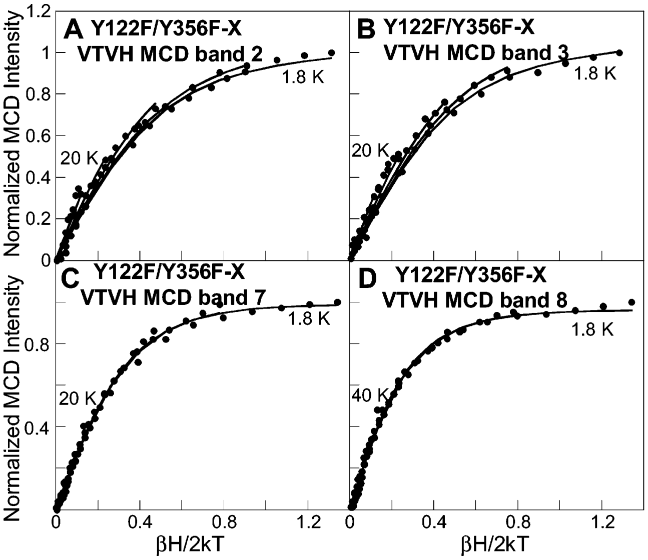

Figure 5. VTVH MCD data of **X** in R2-Y122F/Y356F variant showing unnested saturation behavior within experimental standard deviation: (A) band 2 at 19 230 cm^{-1}, (B) band 3 at 22 220 cm^{-1}, (C) band 7 at 26 810 cm^{-1}, and (D) band 8 at 28 740 cm^{-1} at 1.8, 3.0, 5.0, 10, 20, and 40 K. The magnetization data were fit with a spin Hamiltonian for an $S = {}^1/_2$ ground state Kramer's doublet.[60]

The decayed **X** in the R2-W48A variant is characterized by a broad negative feature at 15 000−20 000 cm^{-1} and a broad positive, temperature independent feature at 25 000−30 000 cm^{-1} which is associated with the diamagnetic decayed diferric cluster. The tyrosyl radical feature is not obvious in this spectrum as it is very weak and masked by the broad negative and positive features. Importantly, the MCD spectra of decayed **X** in Figure S2 clearly display different features from those attributed to **X**. Given that the spin−orbit coupling constant for the tyrosyl radical is small, this at most contributes a small feature to the MCD spectrum of decayed **X**. The MCD features of intermediate **X** assigned as spin flips (bands 4 and 5) in Figure 4 are present even after subtraction of the tyrosyl radical contribution in R2-WT enzyme and are present in the MCD spectrum of Y122F/Y356F-**X**, which does not contain a contribution from the tyrosyl radical (from EPR).

Finally, it is important to note for Figures 3 and 4 that while R2-WT-**X** and R2-Y122F/Y356F-**X** exhibit similar energies for the three spin allowed d−d transitions of the Fe^{IV} center, the d−d transitions in R2-W48A-**X** (Figure 4C) are shifted to higher energy and display a smaller energy separation of bands 1−3.

3.3. Variable Temperature Variable Field (VTVH) MCD. VTVH-MCD data were collected for R2-WT and the two variant forms of intermediate **X**. R2-Y122F/Y356F-**X** displays the most well resolved MCD transitions for VTVH analysis, Figure 4. The VTVH-MCD data for R2-Y122F/Y356F-**X** were collected at four different bands as presented in Figure 5. All the saturation magnetization curves (MCD intensity as a function of $\beta H/2kT$)

---

(75) Brown, C. A.; Remar, G. J.; Musselman, R. L.; Solomon, E. I. *Inorg. Chem.* **1995**, *34*, 688−717.

(76) Jorgensen, K. *Oxidation Numbers and Oxidation States*; Springer-Verlag: New York, 1969.

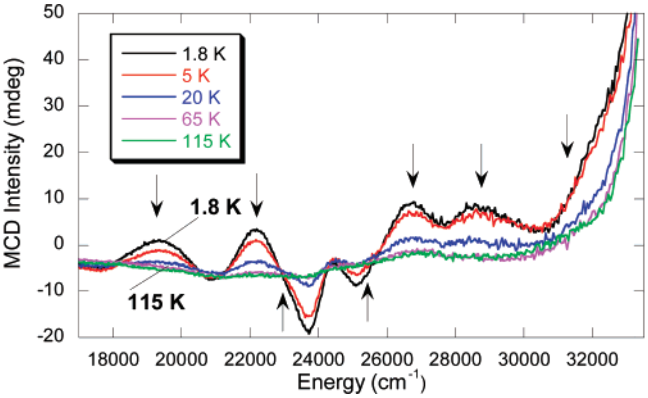

Figure 6. Temperature dependence of MCD signal of intermediate **X** in R2-Y122F/Y356F. All MCD bands decrease in intensity with increase in temperature indicative of *C*-term MCD behavior.

recorded at various magnetic fields and at a series of temperatures from 1.8 to 40 K overlay within standard deviation and thus do not display any nesting behavior. These isotherms are dependent on the S_{tot} of the ground state and were fit using the EPR parameters of **X** ($g_{||} = 2.006$ and $g_{\perp} = 1.994$), resulting in spin Hamiltonian parameters characteristic for an isotropic ground state with an isolated $S = {}^1/_2$ for all bands.

The temperature dependence of the full MCD spectra of **X** for both the R2-Y122F/Y356F and R2-W48A variants, ranging from 1.8 to 170 K at high field (7 T) were collected. Figure 6 shows the 7-T MCD spectrum of intermediate **X** in the R2-Y122F/Y356F variant over the energy region of 17 000−33 000 cm^{-1} between 1.8 and 115 K. The variable temperature MCD data exhibit typical *C*-term behavior with the signal intensity decreasing as $1/T$ with increasing temperature. This behavior is observed for all the spectral features of intermediate **X**.

Since the MCD signal intensity of all bands decreases linearly as $1/T$ for temperatures up to 115 K, it can be concluded that there is no thermally accessible low-lying excited sublevel of the $S_{tot} = {}^1/_2$ ground state of intermediate **X**. The energy splitting of the ground state is described by a phenomenological spin Hamiltonian, $H = -2J\mathbf{S}_1\cdot\mathbf{S}_2$, where **S** represents the spin on each iron and J is the exchange coupling constant. A two-level Boltzmann distribution yields a $\Delta E > 110$ cm^{-1} between the two levels with a population of <20% population of the excited state, at a temperature of 115 K. The lack of an observable thermally accessible (at 115 K) $S_{tot} = {}^3/_2$ excited state indicates a strong antiferromagnetically coupled $Fe^{III}-O-Fe^{IV}$ dimer, giving a lower limit on the magnitude of the exchange coupling of $-3J > 110$ cm^{-1}.

4. Analysis

Our preliminary report on the RFQ-MCD of **X** in Y122F/Y356F used a quantitative assessment of the Fe^{IV} ligand field to support that intermediate **X** contained a single oxo bridge,[38] consistent with $^{17}O-O_2$ and H_2O ENDOR data.[40] The ligand field analysis argued against the possibility of a bis-μ-oxo core structure due to the larger equatorial ligand field oxo bonds which leads to a larger splitting of the Fe^{IV} d−d transitions compared with the mono-μ-oxo splitting. The larger splitting of the bis-μ-oxo would shift the Fe^{IV} d−d transitions to higher energy than the relatively low-energy d−d transitions observed in intermediate **X**. These LF calculations were calibrated based on absorption and MCD data from mono- and bis-μ-oxo binuclear Mn systems.[77−79]

This study extends the initial ligand field analysis to include covalency effects and π- as well as σ-bonding interactions from the bridging oxo ligand(s) through the use of DFT calculations combined with perturbations on the spectral data of **X** in the two variants and WT (section 5). This computational approach was used to explore the electronic and geometric structure differences between three possible structural models for **X** (the mono-μ-oxo, μ-oxo/μ-hydroxo, and bis-μ-oxo bridged species). Furthermore, TD-DFT, Slater, and ΔSCF transition state methods were used to calculate the Fe^{IV} d−d transitions within these three models and correlate their energies and intensities to those observed by RFQ-MCD for intermediate **X** in the WT R2, as well as the structurally perturbed forms of **X** in the two variants (section 5).

4.1. DFT: Geometry Optimizations. Previous structural assignments for intermediate **X** have primarily focused on either a mono- or bis-μ-oxo core structure, based on EPR,[18] ENDOR,[39,40] EXAFS,[37] Mössbauer,[28] and MCD[38] spectroscopies as well as DFT calculations.[33,42−49,51−53,80] The μ-oxo/μ-hydroxo core structure is also included here, as it has been generated in diferric model complexes[81] as well as explored by DFT[51] but has not been considered thus far as a viable structure for intermediate **X**. This structure would have one strong oxo bridge but a short Fe−Fe distance associated with two monoatomic bridging ligands, as observed in EXAFS.[37] The tops of Figures 7−9 display the three possible geometric core structures of intermediate **X** evaluated here: mono-μ-oxo, $[Fe^{III}(\mu\text{-}O)Fe^{IV}]$; μ-oxo/μ-hydroxo, $[Fe^{III}(\mu\text{-}O)(\mu\text{-}OH)Fe^{IV}]$; and bis-$\mu$-oxo, $[Fe^{III}(\mu\text{-}O)_2Fe^{IV}]$, respectively.

While there is a small number of high-valent binuclear iron oxo model systems available, only one has been structurally characterized,[82] and none of these models has the correct high-spin state for each iron as found in intermediate **X**. Therefore, the computational models presented here were based on similar diferric and dimanganese model structures, with an effort to keep the non-oxo ligands identical. The mono-μ-oxo structure was based on the structurally characterized $[(Fe^{III})_2(\mu\text{-}O)([9]\text{-}aneN_3)_2(\mu\text{-}CH_3CO_2)_2]^{3+}$ complex of Wieghardt et al.[83] The electronic structure of this complex consists of two high-spin Fe^{III} ($S = {}^5/_2$) atoms antiferromagnetically coupled to yield an overall $S = 0$ ground state. The DFT geometry optimization of this complex led to a final structure that paralleled the geometric and electronic structure of the actual complex. However, upon the computational removal of one electron from the geometry optimized Fe^{III}_2 complex, the oxidized complex reoptimized to a low-spin Fe^{III} $S = {}^1/_2$ and low-spin Fe^{IV} $S = 1$ antiferromagnetically coupled system. This result is consistent with the

---

(77) Brunold, T. C.; Gamelin, D. R.; Solomon, E. I. *J. Am. Chem. Soc.* **2000**, *122*, 8511−8523.

(78) Brunold, T. C.; Gamelin, D. R.; Stemmler, T. L.; Mandal, S. K.; Armstrong, W. H.; Penner-Hahn, J. E.; Solomon, E. I. *J. Am. Chem. Soc.* **1998**, *120*, 8724−8738.

(79) Gamelin, D. R.; Kirk, M. L.; Stemmler, T. L.; Pal, S.; Armstrong, W. H.; Penner-Hahn, J. E.; Solomon, E. I. *J. Am. Chem. Soc.* **1994**, *116*, 2392−2399.

(80) Han, W. G.; Liu, T. Q.; Lovell, T.; Noodleman, L. *J. Comput. Chem.* **2006**, *27*, 1292−1306.

(81) Stubna, A.; Jo, D. H.; Costas, M.; Brenessel, W. W.; Andres, H.; Bominaar, E. L.; Munck, E.; Que, L. *Inorg. Chem.* **2004**, *43*, 3067−3079.

(82) Hsu, H. F.; Dong, Y. H.; Shu, L. J.; Young, V. G.; Que, L. *J. Am. Chem. Soc.* **1999**, *121*, 5230−5237.

(83) Wieghardt, K.; Pohl, K.; Gebert, W. *Angew. Chem., Int. Ed.* **1983**, *22*, 727−727.

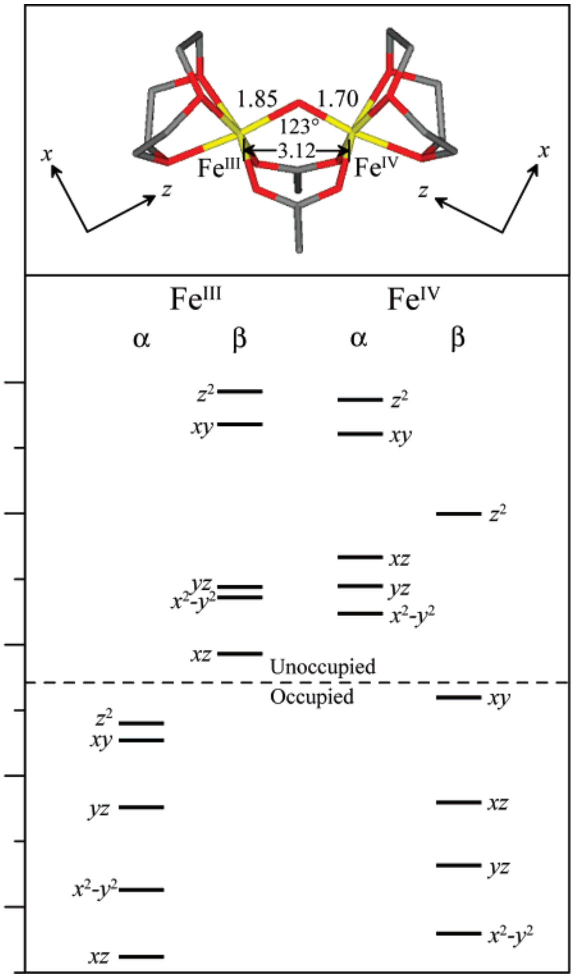

Figure 7. Energy level diagram of the $S_{tot} = {}^1/_2$ unrestricted DFT geometry optimized mono-μ-oxo, [Fe^{III}(μ-O)Fe^{IV}] core structure. The top portion displays the mono-μ-oxo structure with Fe−O and Fe−Fe distance and angle data. Local coordinate frames are displayed for each iron. Ligand hydrogens are omitted for clarity.

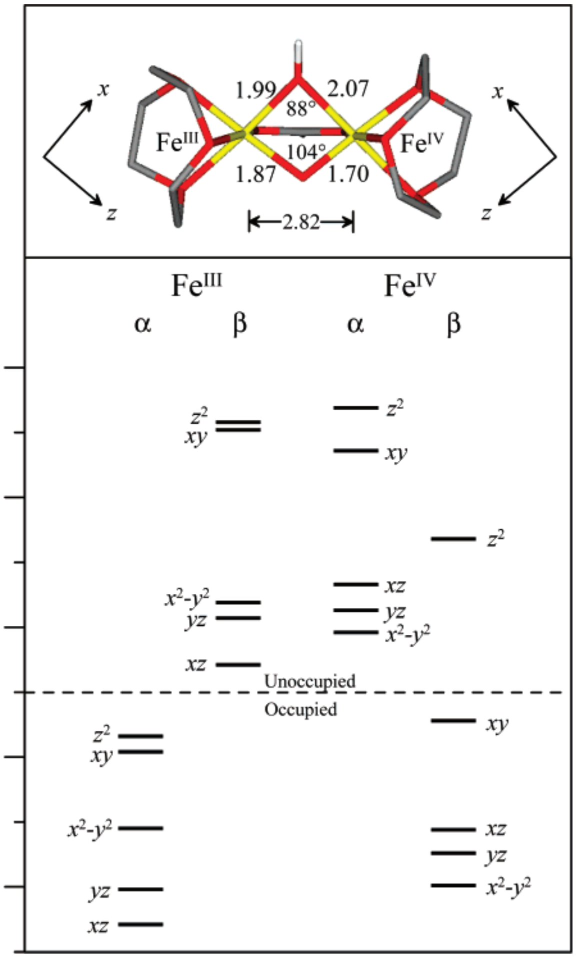

Figure 8. Energy level diagram of the $S_{tot} = {}^1/_2$ unrestricted DFT geometry optimized μ-oxo/μ-hydroxo, [Fe^{III}(μ-O)(μ-OH)Fe^{IV}] core structure. The top portion displays the μ-oxo/μ-hydroxo structure with Fe−O and Fe−Fe distance and angle data. Local coordinate frames are displayed for each iron. Non-oxo ligand hydrogens are omitted for clarity.

experimental electrochemical results for this oxidized complex, which yielded a 35:65 mixture of $S = {}^1/_2$ and $S = {}^3/_2$ species.[84] The Mössbauer and EPR results from this complex were ambiguous as to the nature of the Fe^{IV} spin state.

The μ-oxo/μ-hydroxo and bis-μ-oxo models were based on the structurally characterized [$Mn^{III}(\mu\text{-}O)_2Mn^{IV}([9]aneN_3)_2(\mu\text{-}CH_3CO_2)]^{2+}$ complex and differ by one proton bound to an oxo bridge.[79] Similar spin-state issues (these complexes energetically optimized to a low-spin state on each iron) were also encountered for these models. The Fe^{IV} spin state plays an important role in defining the geometric and electronic structure of the complex, which determines its reactivity. Therefore, a weaker ligand set was chosen for all three structures to maintain high-spin states on both irons and to preserve their structural consistency. The nitrogen-based[9]aneN_3 ligand set was replaced with a weaker oxygen-based 9-crown-3 ether ligand set. This ligand change resulted in the three computational models shown in Figures 7−9. With this ligand modification, all three models geometry optimized to minimum energy complexes, which maintained high-spin Fe^{III} $S = {}^5/_2$ antiferromagnetically coupled to a high-spin Fe^{IV} $S = 2$ to yield $S_{tot} = {}^1/_2$ ground states. The mono-μ-oxo structure was the only complex which needed to be geometry optimized to the ferromagnetic $S_{tot} = {}^9/_2$ state first and then reoptimized under broken symmetry (BS) to converge to the lower energy antiferromagnetically coupled high-spin state. The other structures were also geometry optimized to ferromagnetically coupled $S_{tot} = {}^9/_2$ states, which were at higher energy than the $S_{tot} = {}^1/_2$ state for all three complexes.

4.2. DFT: Ground State Geometric and Electronic Structure. Figures 7−9 display a geometry optimized structure and energy level diagram for each of the three possible structural models of intermediate **X**. The comparison of these calculated structures to the experimental data of intermediate **X** provides a reasonable basis for the evaluation of the geometric and electronic structure of **X**.

While all three structures maintain a high-spin Fe^{III} ($S = {}^5/_2$) and Fe^{IV} ($S = 2$) antiferromagnetically coupled to yield an $S_{tot} = {}^1/_2$ ground state, their geometric and electronic structures vary. The mono-μ-oxo and μ-oxo/μ-hydroxo structures display a shorter Fe^{IV}—O_{oxo} distance of 1.70 Å, while the bis-μ-oxo structure displays two Fe^{IV}—O_{oxo} distances of 1.73 Å. However, all three bridged structures have longer distances than the experimentally well-defined (TMC-NCMe)Fe^{IV}=O ($S = 1$) complex with a terminal oxo, which has a relatively short Fe^{IV}—

---

(84) Slep, L. D.; Mijovilovich, A.; Meyer-Klaucke, W.; Weyhermuller, T.; Bill, E.; Bothe, E.; Neese, F.; Wieghardt, K. *J. Am. Chem. Soc.* **2003**, *125*, 15554−15570.

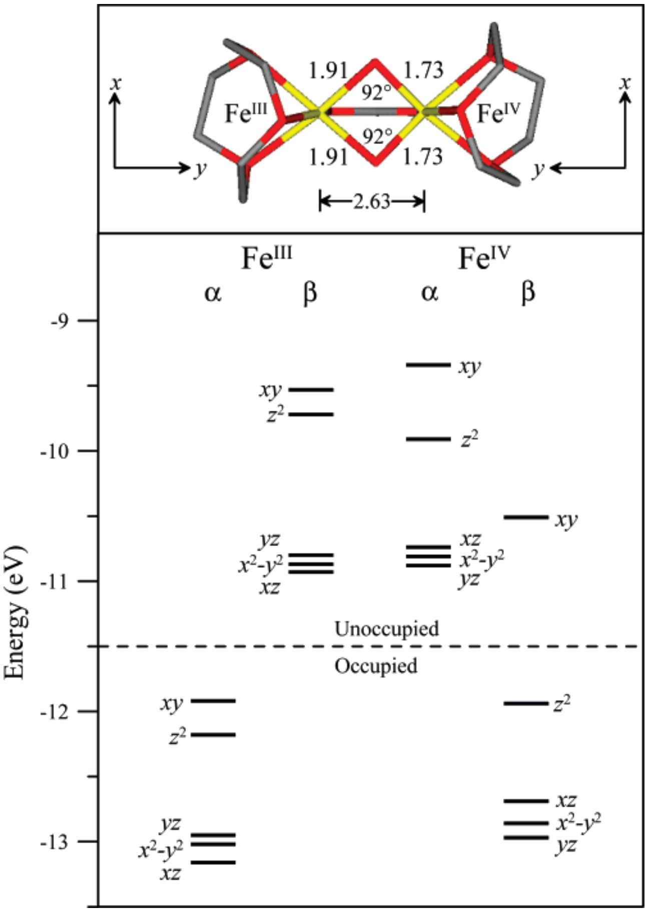

Figure 9. Energy level diagram of the $S_{tot} = {}^1/_2$ unrestricted DFT geometry optimized bis-μ-oxo, $[Fe^{III}(\mu\text{-}O)_2Fe^{IV}]$ core structure. The top portion displays the bis-μ-oxo structure with Fe—O and Fe—Fe distance and angle data. Local coordinate frames are displayed for each iron. Ligand hydrogens are omitted for clarity.

O_{oxo} distance of 1.65 Å.[85] The Fe^{III}—O—Fe^{IV} angle decreases from the mono-μ-oxo to the μ-oxo/μ-hydroxo to the bis-μ-oxo structures: 123°, 104°, and 92° respectively. The Fe^{III}—Fe^{IV} distance also decreases from the mono-μ-oxo to the μ-oxo/μ-hydroxo to the bis-μ-oxo structures: 3.12, 2.82, and 2.63 Å respectively. Parallel to the Fe^{IV}—O_{oxo} distance, the Fe^{III}—O_{oxo} distance also lengthened from the mono-μ-oxo to the μ-oxo/μ-hydroxo to the bis-μ-oxo structures: 1.85, 1.87, and 1.91 Å, respectively.

The geometric differences among the three structures are reflected in their electronic structures. Each electronic structure is given by the energy level diagram at the bottom of Figures 7−9. These figures display the ground state occupied and unoccupied d-orbital energy levels for each iron. The Fe^{IV} has five α unoccupied, four β occupied, and one β unoccupied d orbitals. The Fe^{IV} 10*D*q values (based on the average energy separation between the d-σ^* (xy, z^2) and d-π^* (xz, yz, and x^2-y^2) manifolds for the Fe^{IV} β-orbitals) are 16 100, 14 100, and 13 000 cm^{-1} for the mono-μ-oxo, μ-oxo/μ-hydroxo, and the bis-μ-oxo structures, respectively. The three 10*D*q values vary by only ~3000 cm^{-1}. The energy splittings of the Fe^{IV} d-σ^* orbitals are also fairly similar with energies of 11 300, 11 300, and 11 500 cm^{-1} for the mono-μ-oxo, μ-oxo/μ-hydroxo, and bis-μ-oxo structures, respectively. Importantly, the energy splittings of the Fe^{IV} d-π^* manifold decreased significantly from the mono-μ-oxo to μ-oxo/μ-hydroxo to bis-μ-oxo structures: 8100, 3500, and 2300 cm^{-1} respectively.

The Fe^{III} d-manifolds displayed similar energy changes among the three structures. Interestingly, the Fe^{III} and Fe^{IV} d-manifolds appear in nearly the same energy region for all three structures, which reflects a significant amount of covalency within the Fe^{III}−O−Fe^{IV} unit (*vide infra*).

The Fe^{IV} d-manifold energy differences reflect changes in the bonding interactions between the Fe^{IV} and the core oxo and hydroxo ligand(s). Due to a significant amount of spin polarization in the β-occupied Fe^{IV} d-orbitals, these differences are most easily correlated in the α-unoccupied Fe^{IV} d-orbitals, which reflect the uncompensated bonding interactions of the Fe^{IV} β-occupied orbitals. Figure 10 summarizes these energy differences; also see Tables 2 and 3. Supporting Information Figures S5 and S6 include contours that further dissect the Fe^{IV}−O_{oxo} bonding interactions that give rise to these energy differences. Figure 10 and Tables 2 and 3 also include a hypothetical mononuclear Fe^{IV}═O high-spin $S = 2$ system as a reference.[86,87] Figure 10 displays the large energy splitting between the mononuclear Fe^{IV} d-σ manifold. This is due to dominant Fe^{IV}—O_{oxo} σ-bonding along the z-axis versus the relatively weaker equatorial ligand field along the x and y axes. This is reflected in the large amount of oxo character in the d(z^2) orbital, Tables 2 and 3. In Figure 10b−d and S5, all three binuclear models display a smaller splitting between their Fe^{IV} d-σ^* orbitals, consistent with their longer Fe^{IV}—O_{oxo} bond lengths. Also, the bent Fe^{III}—O—Fe^{IV} angle of 123° in the mono-μ-oxo and 104° in the μ-oxo/μ-hydroxo dimers weakens the Fe^{IV}—O_{p_z} bond and lowers the energy of the d(z^2) orbital in both structures relative to the mononuclear case. (Note that different axis systems are used for the different structures. The z-axis is directed along the Fe^{IV}-oxo bond in the mononuclear, binuclear mono-μ-oxo, and binuclear μ-oxo/μ-hydroxo cases. The z-axis in the binuclear bis-μ-oxo case is perpendicular to the Fe^{IV}—$(O)_2$ plane. The x and y axes bisect the ligand−Fe bonds in the binuclear systems.) The bis-μ-oxo structure has two oxo ligands that impose a stronger equatorial ligand field and increase the energy of the d(xy) orbital. Overall, the Fe^{IV} d-σ^* splitting is smaller for the binuclear complexes due to the bridged bonding of the oxo that results in a weaker Fe^{IV}—Op_z bond. The bent nature of the Fe^{III}—O—Fe^{IV} unit also weakens the Fe^{IV}—O_{p_z} bond in the mono-μ-oxo and the μ-oxo/μ-hydroxo complexes.

Figures 10a and S6a display the large energy splitting of the mononuclear Fe^{IV}═O d-π^* orbitals. This is due to the large amount of oxo $p_{x,y}$ π character in the d(xz) and d(yz) orbitals with none in the d(xy) orbital. Note the mononuclear Fe^{IV} d(xz) and d(yz) orbitals lie close in energy due to the close C_{4v} symmetry resulting in similar oxo π character. However, the d(xz) and d(yz) d-π^* splitting greatly increases, and their average energy decreases in the binuclear mono-μ-oxo Fe^{IV} structure. This is primarily due to the sharing of oxo character within the Fe^{III}—O—Fe^{IV} unit, which elongates the Fe^{IV}—O_{oxo} bond and

---

(85) Rohde, J. U.; In, J. H.; Lim, M. H.; Brennessel, W. W.; Bukowski, M. R.; Stubna, A.; Munck, E.; Nam, W.; Que, L. *Science* **2003**, *299*, 1037−1039.

(86) Decker, A.; Clay, M. D.; Solomon, E. I. *J. Inorg. Biochem.* **2006**, *100*, 697−706.

(87) The high-spin $S = 2$ mononuclear Fe^{IV}═O structure used here is a six-coordinate structure (as in the activated non-heme iron enzymes), consisting of two amines which model histidines, one formate which models glutamate or aspartate, one hydroxide, and one water.

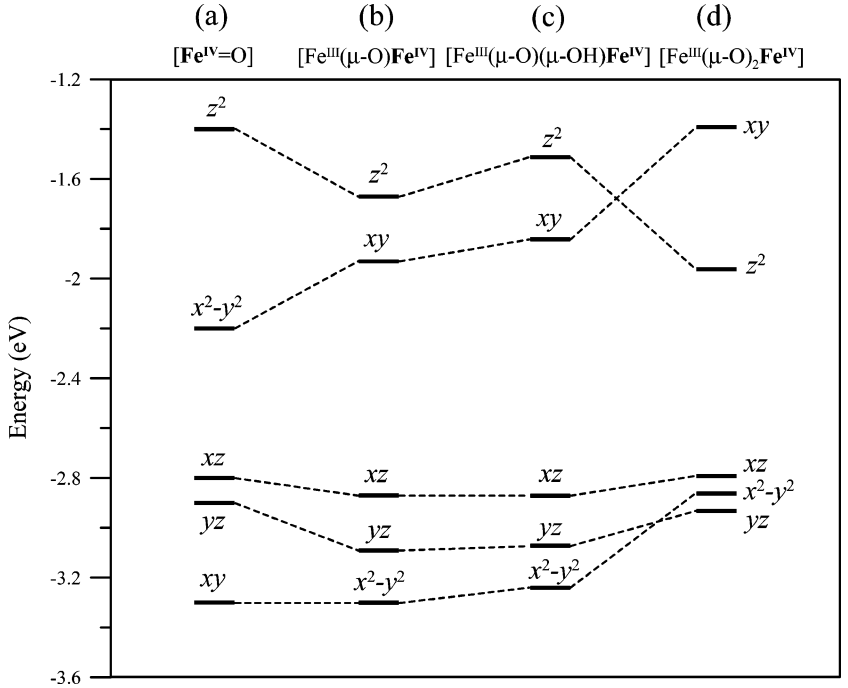

Figure 10. Comparison of the unoccupied α Fe^{IV} d-orbital energy levels between the (a) mononuclear Fe^{IV}=O $S = 2$; (b) mono-μ-oxo, $S_{tot} = {}^1/_2$; (c) μ-oxo/μ-hydroxo, $S_{tot} = {}^1/_2$; and (d) bis-μ-oxo, $S_{tot} = {}^1/_2$ structures.

causes both the d(xz) and d(yz) orbitals to lower in energy. Furthermore, while bending in the xz-plane has little effect on the energy of the d(yz) orbital, the d(xz) orbital loses π overlap but gains σ overlap from the O_{p_x} orbital. This causes an energy stabilization of the d(xz) orbital, while the d(yz) orbital lowers in energy and results in a larger splitting between the two d-orbitals. The Fe^{IV} d(x^2-y^2) orbital in the mono-μ-oxo structure has no oxo overlap and thus no energy change. The μ-oxo/μ-hydroxo structure displays a somewhat smaller total energy splitting within the Fe^{IV} d-π* manifold, which results from the added interaction between the hydroxo π and the d(x^2-y^2) orbital. This is due to a butterfly distortion of the [Fe^{III}(μ-O)(μ-OH)Fe^{IV}] unit, which offsets the oxo p_x orbital and introduces some oxo character into the d(x^2-y^2) orbital, as shown in Figure S6c. The most dramatic energy change occurs within the bis-μ-oxo Fe^{IV} d-π* orbitals (Figure 10d and Tables 2 and 3). In the bis-μ-oxo case, there is less mixing of the Fe^{IV} d-orbitals with Fe^{III} relative to the previous structures and the combined oxo character in the Fe^{IV} increases, which increases the overall d-π* energy. More importantly, the C_{2v} symmetry of the bis-μ-oxo complex provides similar oxo-π contributions to all three d-π* orbitals (from Table 2, the percent oxo character in each of the d-π* orbitals ranges from 26, 20, and 23 in the bis-μ-oxo structure to 21, 20, and 0 in the mono-μ-oxo structure), resulting in similar d-π* energies and thus a much smaller splitting within the bis-μ-oxo Fe^{IV} d-π* manifold, relative to the mono-μ-oxo and μ-oxo/μ-hydroxo bridged structures.

4.3. TD-DFT: Spectral Assignments. Time-Dependent Density Functional Theory (TD-DFT) provided a quantitative prediction of transition energies and intensities, which was applied to all three proposed intermediate **X** models, and the results for the Fe^{IV} ligand field transitions are summarized in Figure 11 and Table 4. Slater and some ΔSCF transition state energies, which converged to the spectral excited states, were also calculated for the three binuclear structures (Table 5) and provided energies similar to the TD-DFT results. The TD-DFT transition energies and intensities of the three possible **X** models were correlated to the experimental data of intermediate **X**.

The TD-DFT Fe^{IV} d−d transitions originate from the promotion of an electron from one of the four β-occupied Fe^{IV} d-orbitals to the β-unoccupied Fe^{IV} d-orbital in Figures 7−9. Figure 11 displays the TD-DFT calculated Fe^{IV} d−d transitions in blue for each structure and an overlay of the WT intermediate **X** Fe^{IV} d−d transitions in red as identified from RFQ-absorption and MCD spectra, in Figures 3 and 4. The results from the excited state analysis were consistent with the ground state splittings described above.

In general, the experimental and calculated spectra can be divided into two energy regions. The lower energy region, <15 000 cm^{-1}, contained a single spin-allowed Fe^{IV} d−d transition in all three calculated structures near 12 000 cm^{-1}, which was attributed to the strong oxo axial ligand field and the relatively weak equatorial ligand field of the mono-μ-oxo and μ-oxo/μ-hydroxo models and the weak axial/strong equatorial ligand field of the bis-μ-oxo model that significantly split the d-σ* orbitals and the transition energy between these orbitals. This d−d transition (the Fe^{IV} d-σ* → d-σ* Jahn−Teller transition) was not observed in the experimental absorption or MCD data of the WT and both variants, which could reflect a weak absorption and very low MCD intensity as it is well separated from the CT transitions and will not mix by spin−orbit coupling, which is required for low-temperature MCD intensity. Also note that related bis-μ-oxo and mono-μ-oxo Mn dimers display Mn^{III} (high-spin d^4, $S_{tot} = 2$) d-σ* → d-σ* Jahn−Teller transitions at 11 000 and 14 500 cm^{-1} respectively, as determined by absorption, CD, and MCD spectroscopies,[78,79] which are close to the calculated Fe^{IV} d-σ* splitting of 12 000 cm^{-1} for all three model structures studied here.

Three spin-allowed Fe^{IV} d−d transitions are observed in the higher energy region, >15 000 cm^{-1} for both experimental and calculated spectra, and they exhibit an energy trend consistent with the ground state analysis. While electronic relaxation effects

Table 2. Energies (eV) and Compositions (%) of the α Unoccupied Fe^{IV} d-Based MOs for Mono- and Binuclear Fe^{IV} (a) Mono-μ-oxo, (b) μ-Oxo/μ-Hydroxo, and (c) Bis-μ-oxo Structures

Mononuclear Fe

MO no.	orbital	*E* (eV)	Fe^{IV}	O
		unoccupied		
α 51	z^2	−1.40	53	17
α 50	x^2-y^2	−2.20	74	3
α 49	xz	−2.80	62	33
α 48	yz	−2.90	62	32
α 47	xy	−3.30	81	0

Binuclear Fe

(a) mono-μ-oxo

MO no.	orbital	*E* (eV)	Fe^{III}	Fe^{IV}	O$_A$
		unoccupied			
α 137	z^2	−13.13	1	62	16
α 136	xy	−13.39	0	71	0
α 135	xz	−14.33	10	53	21
α 134	yz	−14.55	2	71	20
α 133	x^2-y^2	−14.76	0	82	0

(b) μ-oxo/μ-hydroxo

MO no.	orbital	*E* (eV)	Fe^{III}	Fe^{IV}	O$_A$H	O$_B$
		unoccupied				
α 126	z^2	−13.31	1	62	2	16
α 125	xy	−13.64	0	72	7	0
α 124	xz	−14.67	7	57	0	21
α 123	yz	−14.87	3	69	0	22
α 122	x^2-y^2	−15.04	3	75	7	7

(c) bis-μ-oxo

MO no.	orbital	*E* (eV)	Fe^{III}	Fe^{IV}	O$_A$	O$_B$
		unoccupied				
α 126	xy	−9.35	0	60	14	15
α 125	z^2	−9.92	0	68	4	3
α 124	xz	−10.75	2	67	4	22
α 123	x^2-y^2	−10.82	3	67	12	8
α 122	yz	−10.89	1	71	17	6

Table 3. Energies (eV) and Compositions (%) of the β Occupied and Unoccupied Fe^{IV} d-Based MOs for Mono- and Binuclear Fe^{IV} (a) Mono-μ-oxo, (b) μ-Oxo/μ-Hydroxo, and (c) Bis-μ-oxo Structures

Mononuclear Fe

MO no.	orbital	*E* (eV)	Fe^{IV}	O
		unoccupied		
β 51	z^2	−2.70	45	26
		occupied		
β 50	x^2-y^2	−4.60	47	9
β 49	xz	−5.00	34	58
β 48	yz	−5.10	35	52
β 47	xy	−5.60	33	1

Binuclear Fe

(a) mono-μ-oxo

MO no.	orbital	*E* (eV)	Fe^{III}	Fe^{IV}	O$_A$
		unoccupied			
β 135	z^2	−14.00	40	22	18
		occupied			
β 131	xy	−15.40	4	37	0
β 130	xz	−16.20	1	8	4
β 124 (126,122)	yz	−16.68	5	10	13
β 121	x^2-y^2	−17.20	3	19	2

(b) μ-oxo/μ-hydroxo

MO no.	orbital	*E* (eV)	Fe^{III}	Fe^{IV}	O$_A$H	O$_B$
		unoccupied				
β 124	z^2	−14.32	30	30	0	21
		occupied				
β 120	xy	−15.72	6	39	12	1
β 119	xz	−16.56	1	12	1	5
β 116 (115)	yz	−16.74	5	8	2	8
β 114 (112)	x^2-y^2	−16.99	1	12	8	5

(c) bis-μ-oxo

MO no.	orbital	*E* (eV)	Fe^{III}	Fe^{IV}	O$_A$	O$_B$
		unoccupied				
β 124	xy	−10.52	11	37	18	22
		occupied				
β 120	z^2	−11.95	12	31	3	3
β 119	xz	−12.70	4	25	10	40
β 118	x^2-y^2	−12.87	6	24	25	4
β 117	yz	−12.98	3	25	13	12

can be significant, in this case, they were small. The ground state DFT calculations showed that the bis-μ-oxo Fe^{IV} d-π^* β-occupied orbitals were relatively close in energy (split by ∼2300 cm^{-1}), whereas the mono-μ-oxo Fe^{IV} d-π^* β-occupied orbitals were further split in energy (∼8100 cm^{-1}), with the μ-oxo/μ-hydroxo orbitals between the two (∼3500 cm^{-1})(Figures 7−10). This same trend was displayed in the TD-DFT calculations (Figure 11 and Table 4). These three d−d transitions are thus assigned as Fe^{IV} d-π^* → d-σ^* transitions, all originating from the d-π^* manifold. The calculated bis-μ-oxo structure displayed three d-π^* → d-σ^* Fe^{IV} d−d transitions all within a 1800 cm^{-1} region (at 17 500, 18 660, and 19 280 cm^{-1}). The calculated mono-μ-oxo structure displayed its three d-π^* → d-σ^* Fe^{IV} d−d transitions over a 7500 cm^{-1} region (at 18 020, 21 400 and 25 560 cm^{-1}). The μ-oxo/μ-hydroxo structure displayed d-π^* → d-σ^* Fe^{IV} d−d transitions over a range of 3800 cm^{-1} (at 17 900, 19 510, and 21 730 cm^{-1}). Importantly, the experimental RFQ-MCD determined Fe^{IV} d−d transitions for WT intermediate **X** were all within a 4600 cm^{-1} region (at 17 630, 20 080, and 22 260 cm^{-1}).

The Fe^{IV} d−d transition assignment is a crucial step in the correlation of the computational models to the experimental data, and our assignments differ from those presented by Noodleman and co-workers.[53] In the assignment presented here, the spectra are divided into two energy regions: the lower energy region containing the Fe^{IV} Jahn−Teller d-σ^* → d-σ^* transition, not observed experimentally, and the higher energy region containing the three Fe^{IV} d-π^* → d-σ^* transitions. Furthermore, the experimental d-π^* splittings observed have the best correlation to the d-π^* splittings of the calculated μ-oxo/μ-hydroxo model.

In addition to the calculated energies, the TD-DFT results provide oscillator strength information, which can help identify transitions as well as correlate them to the experimental data on intermediate **X**. While the experimental RFQ-absorption and MCD spectra did not display a low-energy Fe^{IV} d-σ^* → d-σ^* Jahn−Teller transition at <15 000 cm^{-1}, the spectra did display three reasonably intense Fe^{IV} d-π^* → d-σ^* transitions in the region >15 000 cm^{-1}. Also, while MCD is important for identifying transitions, the TD-DFT oscillator strengths should be correlated to the absorption intensities. However, the experimental absorption intensities of WT intermediate **X**, as shown in Figure 3A and indicated by the red lines in Figure 11, are not well resolved, and hence the intensities given are not a unique fit. Nevertheless, MCD still has the resolving power to identify and assign bands and give their quantitative energies; the experimental absorption intensities (Figure 11, red) are a

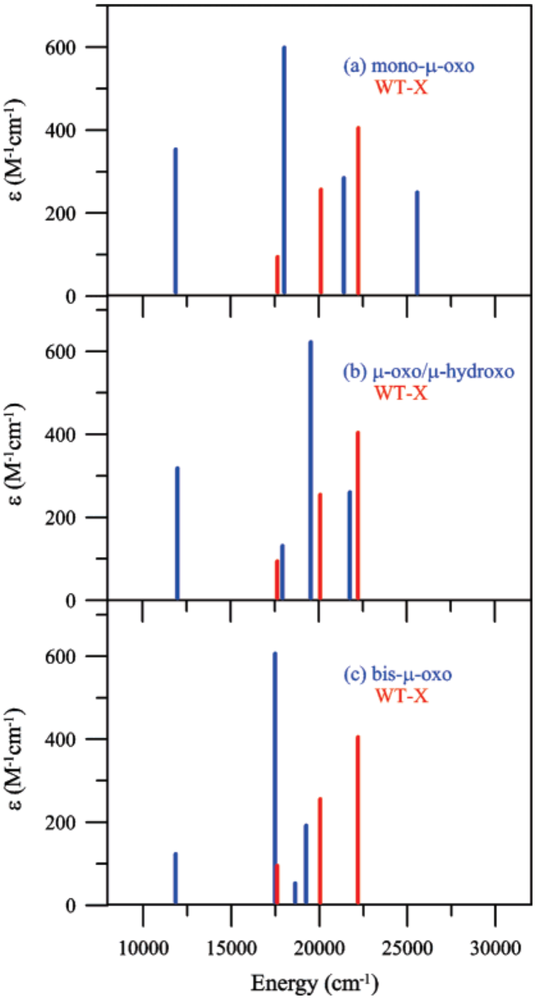

Figure 11. Fe^{IV} d−d transition comparison between the experimental WT−**X** data (red) and the computational TD-DFT data (blue) of the (a) mono-μ-oxo, (b) μ-oxo/μ-hydroxo, and (c) bis-μ-oxo model structures. Each stick represents an Fe^{IV} d−d transition.

reasonable estimate and follow the absorption spectrum for WT intermediate **X** (Figure 3A).

It should also be noted that there were many low-energy MMCT (metal-to-metal charge transfer) transitions in the TD-DFT calculations; see Table S4 in Supporting Information. These transitions are not observed experimentally and would not contribute to the MCD intensity, as MMCTs are unidirectional while MCD requires two perpendicular transition dipole moments. Thus, these transitions are not displayed in Figure 11.[88]

Table 4. TD-DFT Calculated Transition Energies ν_{calc} (cm^{-1}), Oscillator Strength (f), Composition (%), and Dominant One-Electron Excitation of Relevant Fe^{IV} d−d Transitions in (a) Mono-μ-oxo, (b) μ-Oxo/μ-Hydroxo, and (c) Bis-μ-oxo Structures

(a) mono-μ-oxo

ν_{calc} (cm^{-1})	f	%	Fe^{IV} one-electron excitation
11 871	0.0010	62	xy (β 131) → z^2 (β 135)
18 021	0.0017	41	xz (β 130) → z^2 (β 135)
21 404	0.0008	69	yz (β 124) → z^2 (β 135)
25 562	0.0007	55	$x^2{-}y^2$ (β 121) → z^2 (β 135)

(b) μ-oxo/μ-hydroxo

ν_{calc} (cm^{-1})	f	%	Fe^{IV} one-electron excitation
11 946	0.0027	64	xy (β 120) → z^2 (β 124)
17 905	0.0011	46	xz (β 119) → z^2 (β 124)
19 512	0.0053	55	yz (β 116) → z^2 (β 124)
21 730	0.0022	18	$x^2{-}y^2$ (β 114) → z^2 (β 124)

(c) bis-μ-oxo

ν_{calc} (cm^{-1})	f	%	Fe^{IV} one-electron excitation
11 858	0.0003	83	z^2 (β 120) → xy (β 124)
17 507	0.0017	42	xz (β 119) → xy (β 124)
18 660	0.0001	83	yz (β 118) → xy (β 124)
19 283	0.0005	76	$x^2{-}y^2$ (β 117) → xy (β 124)

Table 5. Calculated Slater and ΔSCF Transition Energies ν_{calc} (cm^{-1}) and Designated Fe^{IV} d−d Transition in (a) Mono-μ-oxo, (b) μ-Oxo/μ-Hydroxo, and (c) Bis-μ-oxo Structures

(a) mono-μ-oxo

Slater, ν_{calc} (cm^{-1})	ΔSCF, ν_{calc} (cm^{-1})	Fe^{IV} d–d excitation
13 187	12 918	xy (β 131) → z^2 (β 135)
19 664	19 222	xz (β 130) → z^2 (β 135)
21 349	21 053	yz (β 126) → z^2 (β 135)
24 479	unconverged	$x^2{-}y^2$ (β 125) → z^2 (β 135)

(b) μ-oxo/μ-hydroxo

Slater, ν_{calc} (cm^{-1})	ΔSCF, ν_{calc} (cm^{-1})	Fe^{IV} d–d excitation
12 550	12 226	xy (β 120) → z^2 (β 124)
18 946	18 457	xz (β 119) → z^2 (β 124)
20 253	19 983	yz (β 116) → z^2 (β 124)
22 696	unconverged	$x^2{-}y^2$ (β 114) → z^2 (β 124)

(c) bis-μ-oxo

Slater, ν_{calc} (cm^{-1})	ΔSCF, ν_{calc} (cm^{-1})	Fe^{IV} d–d excitation
13 437	13 350	z^2 (β 120) → xy (β 124)
18 381	18 469	xz (β 119) → xy (β 124)
19 970	unconverged	yz (β 118) → xy (β 124)
20 333	unconverged	$x^2{-}y^2$ (β 117) → xy (β 124)

The TD-DFT results displayed some agreement with the intensities of the higher energy Fe^{IV} d-π^* → d-σ^* transitions. However, the mono-μ-oxo and μ-oxo/μ-hydroxo structures displayed unreasonably large low-energy Fe^{IV} d-σ^* → d-σ^* Jahn−Teller transition TD-DFT intensities due to borrowing from nearby intense MMCT transitions that strongly contribute to the calculated absorption intensities. Therefore, we turn to group theory to gain insight into the Fe^{IV} d−d transition intensities for the different possible structures for **X**. Figure 12 gives the predicted intensities for the mono-μ-oxo and μ-oxo/μ-hydroxo structures. Both structures follow a similar dissent in symmetry starting from a mononuclear high-spin Fe^{IV} in O_h symmetry that is lowered to C_{4v} due to the strong Fe^{IV}-oxo bond (in an oxo monomer or a linear $Fe^{IV}{-}O{-}Fe^{III}$ dimer). In C_{4v} symmetry only one Fe^{IV} d−d transition is orbitally allowed, $^5A_1$ → ^5E(e → a_1), and should have significant absorption intensity. Upon bending of the $Fe^{IV}{-}O{-}Fe^{III}$ dimer, the effective symmetry is lowered to C_s and all four spin-allowed d−d transitions become orbitally allowed; however the most intense transitions will arise from the $^5A_1$ → ^5E(e → a_1) C_{4v} parent transition. Thus, group theory predicts the mono-μ-oxo and the μ-oxo/μ-hydroxo cases will display four orbital- and spin-

---

(88) While the bis-μ-oxo and μ-oxo/μ-hydroxo structures displayed dominant and clear Fe^{IV} d−d transitions in the TD-DFT and Slater transition state calculations, the mono-μ-oxo structure had larger spin-polarization effects that complicate the assignment of specific transitions. However, analysis of the individual molecular orbitals and transitions for the mono-μ-oxo structure allowed the identification of all four Fe^{IV} d−d transitions. In the cases where spin polarization had mixed an Fe^{IV} d-orbital into several transitions, an average energy is given for these transitions, Table 3.

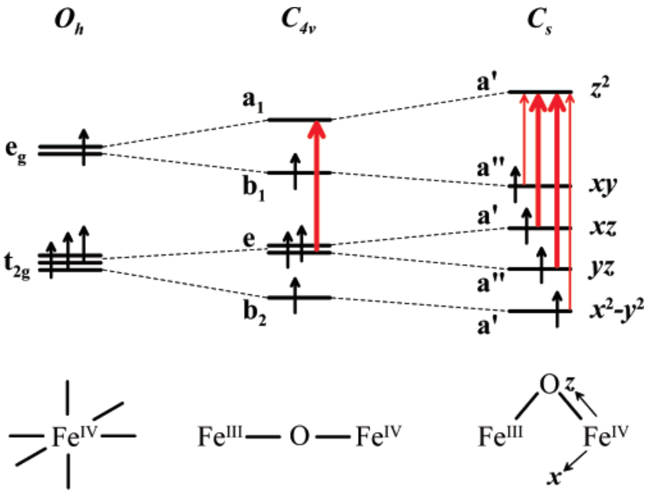

Figure 12. Qualitative splitting of Fe^{IV} d-orbitals mono-μ-oxo and μ-oxo/μ-hydroxo under dissent in symmetry. There are four spin-allowed d−d transitions. The thick red arrows represent Fe^{IV} d−d transitions which are predicted to be more intense than the d−d transitions with thin red arrows, due to the lowering of symmetry.

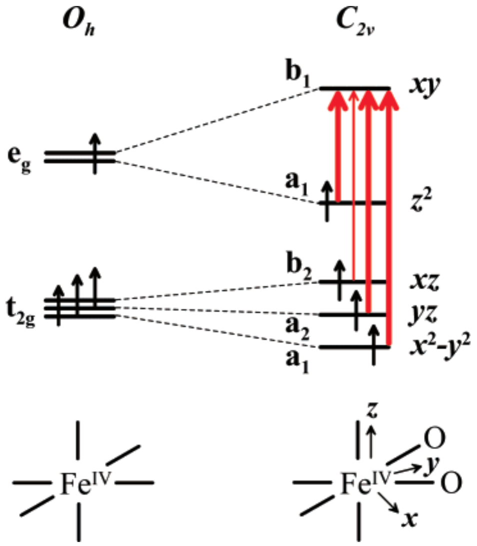

Figure 13. Qualitative splitting of bis-μ-oxo Fe^{IV} d-orbitals under dissent in symmetry. There are four spin-allowed d−d transitions. The thick red arrows represent Fe^{IV} d−d transitions which are orbitally allowed in C_{2v}. The thin red arrow becomes allowed, due to the lowering of symmetry.

allowed d−d transitions, with the two inner d-π* transitions being more intense (Figure 12).

The bis-μ-oxo case is given in Figure 13, with the two cis oxo ligands that lower the Fe^{IV} symmetry to C_{2v} and the d-orbitals split accordingly. Group theory predicts three orbitally allowed transitions in the bis-μ-oxo structure, one d-σ* and two d-π* → d-σ*. If the symmetry is further lowered, the fourth spin-allowed d-π* transition can borrow intensity, yielding three moderately intense d−d transitions with a weaker transition in the middle.

While the lowest energy Jahn−Teller transition, Fe^{IV} d-σ* → d-σ*, was not experimentally observed, group theory predicts the lowest energy Jahn−Teller transition, Fe^{IV} d-σ* → d-σ*, to have significant intensity in the bis-μ-oxo structure but little intensity in the mono-μ-oxo and μ-oxo/μ-hydroxo structures (Figures 11 and 12). Thus, the group theory intensity prediction is also consistent with the μ-oxo/μ-hydroxo but not the bis-μ-oxo structure.

In summary, the energy and intensity comparison of the TD-DFT calculated Fe^{IV} d−d transitions (blue) with the RFQ-absorption and MCD spectra of WT **X** (red) in Figure 11 and Tables 1 and 4 best correlate with and strongly support the μ-oxo/μ-hydroxo structure for intermediate **X**. The Slater transition energies in Table 5 are consistent with the TD-DFT results and also agree with the μ-oxo/μ-hydroxo model. This is further supported by the structural perturbations as described below.

5. Structural Perturbations of X

The variations of the Fe^{IV} d−d transitions in the RFQ-MCD spectra of Figure 4 from the WT and the two variants further support the μ-oxo/μ-hydroxo model and indicate that the Fe remote to Y122 is the Fe^{IV} center. Previous Mössbauer[41] and MCD[26] studies also suggested that the Fe^{IV} is remote to Y122.

The calculated TD-DFT and Slater transition energy separation between the two lowest energy Fe^{IV} d−d transitions (the Jahn−Teller d-σ* → d-σ* transition and the lowest d-π* → d-σ* transition) was ~6000 cm^{-1} for all three structures. This large energy separation does not correlate to the WT or any variant Fe^{IV} band 1−band 2 energy separation and further substantiates that the three observed RFQ-MCD transitions all originate from the Fe^{IV} d-π* manifold. Furthermore, Figure 4 shows that all three Fe^{IV} d−d transitions shift in unison, which would not be possible if band 1 in the RFQ-MCD spectra was assigned as the Jahn−Teller transition. As the d-σ*−d-σ* splitting increases, the d-π*−d-π* splitting would also increase. Thus, if band 1 was the d-σ* transition and band 2 was the lowest energy d-π* transition, the splitting between bands 1 and 2 would decrease, which is not observed between the WT and variant RFQ-MCD spectra. Therefore, the three identified spin-allowed Fe^{IV} d−d transitions in the RFQ-MCD spectra of **X** for the WT and the W48A and Y122F/Y356F variants directly reflect the splitting of the Fe^{IV} d-π* manifold. The total Fe^{IV} d-π* manifold splitting is 4630 cm^{-1} for the WT−**X** (bands 1−3 at 17 630, 20 080, and 22 260 cm^{-1}), whereas the manifold decreases to 2980 cm^{-1} in the W48A variant (19 680, 21 590, and 22 660 cm^{-1}) and increases to 5400 cm^{-1} in the Y122F/Y356F variant (16 700, 19 460, and 22 100 cm^{-1}). The TD-DFT calculated energy separation of the d-π* manifold is ~7400 cm^{-1} for the mono-μ-oxo structure, ~3800 cm^{-1} for the μ-oxo/μ-hydroxo structure, and ~1900 cm^{-1} for the bis-μ-oxo structure. In addition, while the W48A variant exhibited the smallest splitting of the Fe^{IV} d-π* manifold, it was still significantly larger than the splitting calculated for the bis-μ-oxo model.

These large changes in the Fe^{IV} d-π* manifold can be correlated to perturbations of **X** through structural changes that occur in response to the substitutions. Figure 14 displays the proposed structural perturbations of **X** that correlate with the Fe^{IV} d-π* manifold splitting for the WT and two variants. The proposed structure for WT intermediate **X** is shown in Figure 14B with the μ-oxo/μ-hydroxo core structure with the Fe^{III} coordinated by a terminal hydroxide and a monodentate D84 that H-bonds to the −OH of Y122. However, in the proposed structure for Y122F/Y356F−**X** (Figure 14A), the replacement of tyrosine with phenylalanine disrupts this H-bonding network, which would result in the D84 carboxylate and the terminal hydroxide donating more charge to the Fe^{III}. This in turn would

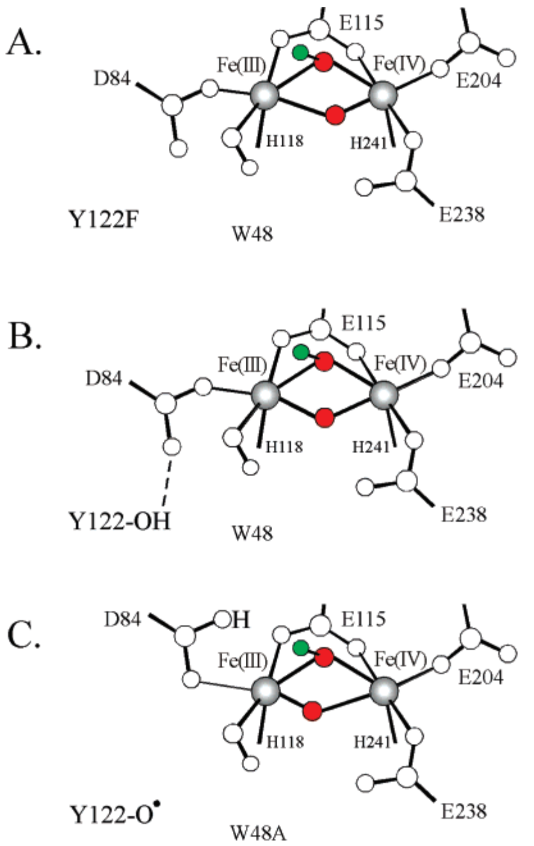

Figure 14. Proposed structural perturbations of **X** in (A) Y122F/Y356F, (B) WT, and (C) W48A variants. The μ-oxo/μ-hydroxo core structure of **X** is composed of oxygen atoms that derive from O_2 colored red and a proton colored green.

weaken the $Fe^{III}-O_{oxo}$ bond and thus strengthen the $O_{oxo}-Fe^{IV}$ bonding, which would result in a larger splitting of the Fe^{IV} d-π* manifold, as observed in the MCD spectrum in Figure 4B. It is important to note that if the Fe closest to Y122 were the Fe^{IV}, then the predicted trend would be opposite to what is experimentally observed.

The W48A variant forms **X** by oxidizing Y122 to Y122$^{\bullet}$, which would also disrupt the H-bonding network (Figure 14C) but by a different mechanism than in the case of the Y122F/Y356F variant. In this case, the proton from Y122−OH could be transferred in a PCET process either to the terminal hydroxide or to the D84 carboxylate and result in the donation of less charge to the Fe^{III} bond by these ligands. This change would, in turn, strengthen the $Fe^{III}-O_{oxo}$ bond and weaken the $O_{oxo}-Fe^{IV}$ bonding, which would result in a smaller splitting of the Fe^{IV} d-π* manifold, as observed in the MCD spectrum in Figure 4C. Again, the opposite trend would be observed if Fe^{IV} was proximal to Y122.

The structural and related spectroscopic perturbations associated with these substitutions also help in the evaluation and exclusion of the possibility of a bis-μ-oxo structure for intermediate **X**. The bis-μ-oxo structure is relatively symmetric and thus would maintain a reasonably small splitting of its Fe^{IV} d-π* manifold. Previous studies on a related bis-μ-oxo $Mn^{III}-Mn^{IV}$ dimer suggest that core bending or butterfly distortion reduces Mn-oxo overlap as observed in its absorption spectrum.[79] Therefore, an increased butterfly distortion of the $Fe^{III}-(\mu\text{-O})_2-Fe^{IV}$ bis-μ-oxo core would decrease the Fe-oxo overlap, which would further decrease the splitting of the d-π* manifold, making correlation to the WT **X** Fe^{IV} d−d transitions worse and explanation of the larger d-π* splitting in the Y122F/Y356F **X** variant even more problematic.

Thus, from these correlations, it appears that the substitutions of Y122F/Y356F and W48A directly perturb the Fe^{III} site of **X**, which indirectly perturbs Fe^{IV} through the oxo bond. This analysis supports the Mössbauer and MCD results that Fe^{IV} is the remote iron center located distal to Y122 and further supports the μ-oxo/μ-hydroxo core structure for intermediate **X**. It also raises important mechanistic implications for the geometric and electronic structure of **X**, as discussed below.

6. Discussion

Through the correlation of EPR, absorption, MCD, and VTVH MCD spectroscopies with DFT and TD-DFT calculations, we have determined that the μ-oxo/μ-hydroxo core structure $[Fe^{III}(\mu\text{-O})(\mu\text{-OH})Fe^{IV}]$ best correlates to the experimental data for the electronic and geometric structure of **X**. The variants perturb the Fe closest to Y122, in a manner which is opposite to what is observed in the spectral changes of Fe^{IV}. This supports a structure where Fe^{IV} is remote to Y122 and is perturbed through the mono-μ-oxo bridge. The geometric and electronic structure characterization of intermediate **X** provides a greater understanding of its reactivity in RNR and further insight into the factors that tune its O_2 reactivity relative to the other binuclear non-heme iron enzymes.

The R2 binuclear non-heme ferrous site reacts with O_2 to ultimately generate a radical on Y122 through intermediate **X**. Scheme 2 presents two possible mechanistic pathways by which the previously established *cis*-μ1,2-peroxo diferric structure[23,36] could convert to intermediate **X**. These two pathways both result in cleavage of the O−O bond; however, the upper pathway is triggered by the protonation of the peroxide. Past studies on the *cis*-μ1,2-peroxo diferric structure show it is activated for protonation.[23,89] Once protonated, the hydroperoxo would raise the potential of the complex and lower the energy of the peroxo σ* orbital, activating it to oxidize one electron from the remote Fe^{III} and the other from the tryptophan residue (W48 in *E. coli* R2) to promote the two-electron reduction and cleavage of the O−O bond, thus forming a μ-oxo/μ-hydroxo $[Fe^{III}(\mu\text{-O})(\mu\text{-OH})Fe^{IV}]$ core structure for intermediate **X**. If the peroxo was not protonated, it is possible that it could rearrange to a μ-η^2:η^2 structure and undergo homolysis of the O−O bond to form the bis-μ-oxo structure. Our experimental results strongly support a μ-oxo/μ-hydroxo core structure with the protonation step activating O−O bond cleavage.

Our data and structural assignment of **X** are in reasonable agreement with previous ^{1,2}H and ^{17}O ENDOR studies of **X** by the Hoffman and Stubbe groups that display two different ^{17}O peaks from $^{17}O_2$ (and a ^{1,2}H peak from $^{1,2}H_2O$) that have been assigned to a single oxo bridge and a terminal hydroxo on Fe^{III}.[39,40] However, our RFQ-MCD data are more consistent with a bridging rather than a terminal hydroxo, which would also be more consistent with the EXAFS Fe−Fe distance.[37] Consistent with our MCD results, the ENDOR data do not support a bis-μ-oxo "diamond core" structure for **X**.

Recently, Noodleman and co-workers proposed a bis-μ-oxo "diamond core" structure for **X** based on the correlation of Fe^{IV}

---

(89) Brunold, T. C.; Tamura, N.; Kitajima, N.; Moro-oka, Y.; Solomon, E. I. *J. Am. Chem. Soc.* **1998**, *120*, 5674−5690.

Scheme 2. Possible O_2 Cleavage Pathways to Generate the High-Valent Intermediate **X**[a]

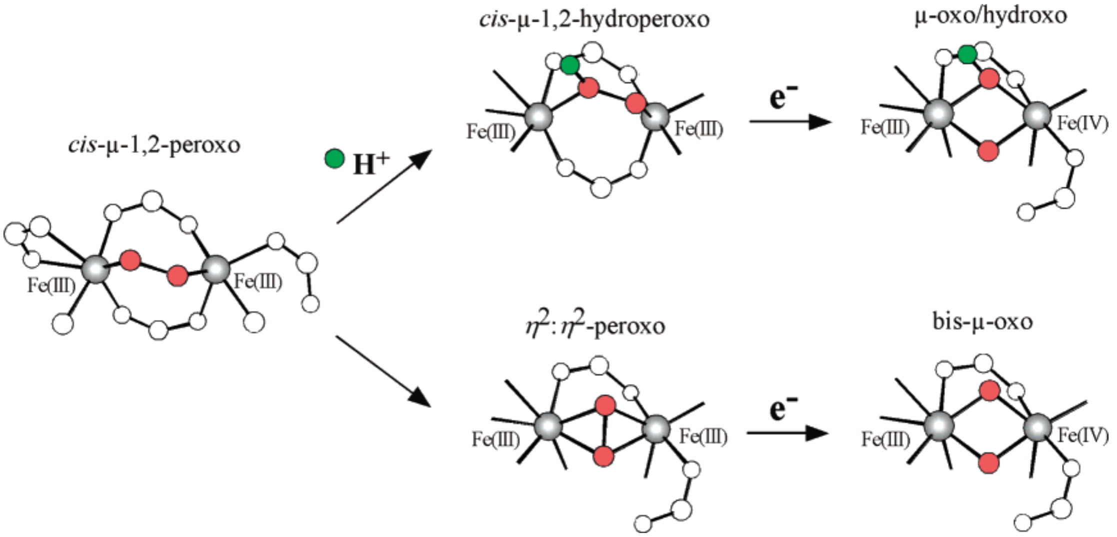

[a] (Top) Proton-triggered and (bottom) non-proton-triggered. Both pathways derive one electron from an exogenous source and the other electron from the remote Fe.

d−d transitions calculated from ΔSCF and Slater transition state methods of four possible models with a truncated binuclear iron active site and the experimentally determined Fe^{IV} d−d transitions from our RFQ-MCD spectrum of **X** in the Y122F/Y356F variant.[53] This variant displays three Fe^{IV} spin-allowed d−d transitions with the largest d−d energy splittings of the three investigated species of intermediate **X**. A comparison of Noodleman's Slater transitions to our TD-DFT and Slater transitions show similar energy splittings for the mono-μ-oxo, μ-oxo/μ-hydroxo, and bis-μ-oxo structures, despite ligand differences between their structures relative to those used here (Figures 7−9). They correlate the lowest energy Jahn−Teller d-σ^* → d-σ^* transition to band 1 in our MCD spectrum. However, all three observed MCD bands shift in unison from the WT transitions to the perturbed W48A and Y122F/Y356F variant transitions. Since the Jahn−Teller transition would shift in a manner opposite to the d-π^* manifold, this means that all three experimentally observed Fe^{IV} d−d transitions must arise from the d-π^* manifold. Alternatively, the energy differences for the higher energy d-π^* transitions of their μ-oxo/μ-hydroxo and mono-μ-oxo models in ref 53 correlate much closer (than the d-π^* transitions of their bis-μ-oxo structure) to the RFQ-MCD spectrum of WT intermediate **X**.

The electronic and geometric structures of **X** in Figures 15 and 16, respectively, are well tuned to oxidize Y122 by one electron, likely via a proton-coupled electron transfer (PCET) process. Figure 16 shows the H-bonding interaction between D84 and Y122−OH, which would provide a superexchange pathway to the proximal Fe^{III}. The electron would then transfer to the lowest energy unoccupied orbital on Fe^{III}. The mono-μ-oxo bridge would then play an important role in electron transfer from Fe^{III} to the remote Fe^{IV}. Figure 15B shows the LUMO (β-124) of the μ-oxo/μ-hydroxo core structure [$Fe^{III}(\mu\text{-O})(\mu\text{-OH})Fe^{IV}$], which displays a good π/σ superexchange pathway between the Fe^{III} d(xz) and the Fe^{IV} (dz^2). This bent μ-oxo superexchange pathway provides an efficient and favorable path for the electron transfer from Y122 through the Fe^{III} to the remote Fe^{IV}, as shown in Figure 16.

In addition, there would be fundamental reactivity differences between the μ-oxo/μ-hydroxo and bis-μ-oxo structures in H atom abstraction from Y122. In contrast to the μ-oxo/μ-hydroxo, the bis-μ-oxo structure contains an extremely poor ET pathway within the $Fe^{III}(\mu\text{ -O})_2Fe^{IV}$ unit to transfer an electron from Y122

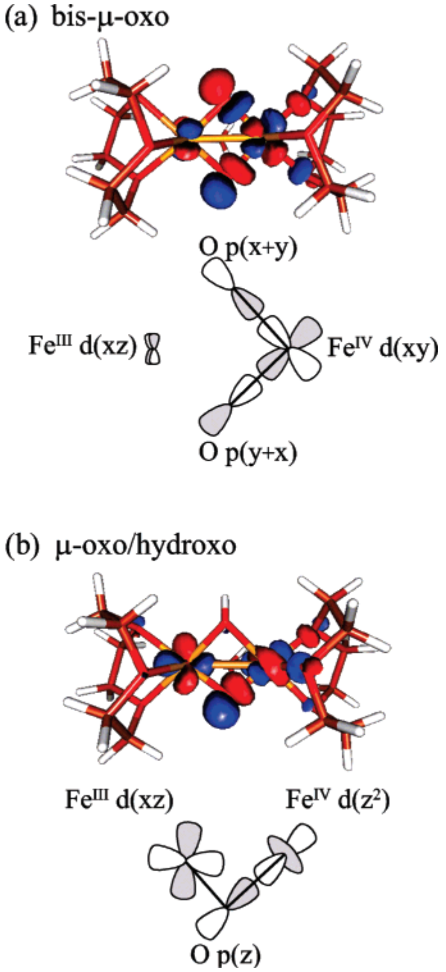

Figure 15. Electron-transfer pathways for the LUMO (β-124) of both the (A) bis-μ-oxo and (B) μ-oxo/μ-hydroxo structures. The bis-μ-oxo structure does not show a good ET pathway, whereas the μ-oxo/μ-hydroxo structure displays a good π/σ superexchange ET pathway.

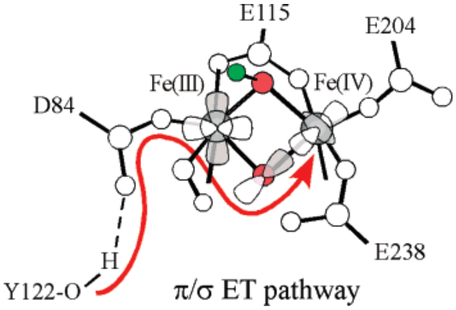

Figure 16. Proposed ET pathway from Y122 to the remote Fe^{IV} through the π/σ superexchange pathway of the μ-oxo bridge.

to the remote Fe^{IV}, as shown in Figure 15A. In contrast to the μ-oxo/μ-hydroxo structure, which has a highly delocalized orbital pathway between Fe^{III} and Fe^{IV}, the bis-μ-oxo structure localizes the LUMO on the remote Fe^{IV} and provides a poor superexchange pathway between Y122 near Fe^{III} and the remote Fe^{IV}.

It is interesting to compare the reactivity of R2 to that of another binuclear non-heme iron protein, hemerythrin. In hemerythrin, O_2 reversibly binds to one Fe, yet there is ET from the second Fe through a bent mono-μ-oxo bridge.[4,5] Again, it has been shown that the π/σ superexchange pathway associated with the bent oxo bridge allows ET to the remote Fe. The bent μ-oxo bridge also plays a dominant role in the exchange coupling of bent ferric oxo dimer sites in both proteins and model complexes, and these studies connect the π/σ exchange coupling in the homo dimers to the superexchange pathway for ET through the bent μ-oxo bridge.[75,77]

In summary, the spectroscopic and computational studies presented here support a μ-oxo/μ-hydroxo [Fe^{III}(μ-O)(μ-OH)-Fe^{IV}] core structure for intermediate **X** and the fact that this core structure is well tuned to provide an efficient and favorable π/σ superexchange pathway for PCET from Y122 to the remote Fe^{IV} to generate the catalytically essential tyrosyl radical in class I RNR.

Acknowledgment. We thank Brian Hoffman for his helpful ENDOR discussions of intermediate **X**. We thank financial support by the NSF Molecular Biophysics Program (MCB-342807 to E.I.S.), NIH (GM-55365 to J.M.B., Jr.), and NIH R.L. Kirschstein NRSA Fellowship (GM-70292 to M.D.C.).

Supporting Information Available: Absorption and MCD spectra of decayed **X**, MCD spectra of **X** trapped using liquid N_2 and isopentane, Fe^{IV} d-orbital energy level diagram for the three models with contours, DFT calculation coordinates for the three models and TD-DFT transition energies, oscillator strengths and M.O. transition assignment for all three models, and the complete ref 71 citation. This material is available free of charge via the Internet at http://pubs.acs.org.

JA070909I